ARTICLE

doi:10.1038/nature25143

Enhancing mitochondrial proteostasis reduces amyloid-β proteotoxicity

Vincenzo Sorrentino[1], Mario Romani[1]*, Laurent Mouchiroud[1]*, John S. Beck[2], Hongbo Zhang[1], Davide D'Amico[1], Norman Moullan[1], Francesca Potenza[1], Adrien W. Schmid[3], Solène Rietsch[1], Scott E. Counts[2] & Johan Auwerx[1]

Alzheimer's disease is a common and devastating disease characterized by aggregation of the amyloid-β peptide. However, we know relatively little about the underlying molecular mechanisms or how to treat patients with Alzheimer's disease. Here we provide bioinformatic and experimental evidence of a conserved mitochondrial stress response signature present in diseases involving amyloid-β proteotoxicity in human, mouse and *Caenorhabditis elegans* that involves the mitochondrial unfolded protein response and mitophagy pathways. Using a worm model of amyloid-β proteotoxicity, GMC101, we recapitulated mitochondrial features and confirmed that the induction of this mitochondrial stress response was essential for the maintenance of mitochondrial proteostasis and health. Notably, increasing mitochondrial proteostasis by pharmacologically and genetically targeting mitochondrial translation and mitophagy increases the fitness and lifespan of GMC101 worms and reduces amyloid aggregation in cells, worms and in transgenic mouse models of Alzheimer's disease. Our data support the relevance of enhancing mitochondrial proteostasis to delay amyloid-β proteotoxic diseases, such as Alzheimer's disease.

Ageing is often accompanied by the onset of proteotoxic degenerative diseases, characterized by the accumulation of unfolded and aggregated proteins. Amyloid diseases are proteotoxic disorders that can affect the nervous system, which is the case in Alzheimer's disease (AD), the most common form of dementia[1]. However, amyloid diseases can also affect other organs, such as is seen in amyloidosis-associated kidney disease[2] and inclusion body myositis[3]. To date, no efficient therapy is available for AD[4], a disease with a strong component of amyloid-β (Aβ) aggregation[1]. Clinical trials for AD have focused primarily on counteracting Aβ aggregation in the brain, which is considered the key pathogenic mechanism[5]. However, AD is a complex, multifactorial disease[6] and mitochondrial dysfunction has been shown to be a common pathological hallmark[7]. Mitochondrial abnormalities in AD include decreased mitochondrial respiration and activity and alterations in mitochondrial morphology[7]. However, the relevance of other aspects of mitochondrial homeostasis, such as mitochondrial proteostasis, to the pathogenesis of AD is still mostly unknown.

Mitochondrial function pathways are disrupted in AD

We analysed brain expression datasets from patients with AD (GN327, GN328 and GN314) archived in GeneNetwork (http://www.genenetwork.org/webqtl/main.py) to define the mitochondrial signature associated with the disease. Gene set enrichment analysis of datasets from healthy individuals versus patients with AD from prefrontal cortex, primary visual cortex and whole brain showed that downregulation of mitochondrial oxidative phosphorylation (OXPHOS) and disruption of mitochondrial import pathways were hallmarks of AD (Fig. 1a, Extended Data Fig. 1a–c, e, f and Supplementary Tables 1–4). Because these processes are linked with and affect mitochondrial proteostasis[8], we used comprehensive gene sets for two major mitochondrial quality control pathways, the mitochondrial unfolded protein response (UPR^{mt}) and mitophagy, to evaluate whether their expression is co-regulated in patients with AD (Supplementary Table 5). Whereas we observed a strong correlation between genes associated with UPR^{mt} and mitophagy in all brain datasets investigated (Fig. 1b and Extended Data Fig. 1d, g), other stress pathways, such as the endoplasmic reticulum stress (UPR^{ER}) response and heat shock response (HSR), were co-regulated to a lesser degree.

Evidence for a mitochondrial stress signature in AD

We next measured UPR^{mt}, mitophagy and OXPHOS transcripts in the human cortex. We have previously reported that several UPR^{mt} genes were upregulated during frank familial or sporadic AD[9]. Here, we extend that analysis and observe that, compared to subjects with no cognitive impairment, several UPR^{mt} and mitophagy transcripts were upregulated in patients with mild cognitive impairment, a putative prodromal stage of AD[10], and in mild and moderate AD (Fig. 1c and Supplementary Table 6), whereas OXPHOS genes were downregulated, consistent with our gene set enrichment analysis. The induction of this mitochondrial stress response was also observed at the protein level in subjects with mild cognitive impairment and AD (Fig. 1d and Extended Data Fig. 1h). The occurrence of this disruption already in patients with mild cognitive impairment suggests that mitochondrial dysfunction contributes to neuron and synapse loss, and that mitochondrial stress pathways may be activated as a protective response during disease progression[10]. We also analysed cortex samples of wild-type and a transgenic mouse model of AD (3×TgAD mice)[11] (Extended Data Fig. 2a), at six and nine months of age. Both mitochondrial quality control and OXPHOS genes were induced in mice with AD (Fig. 1e and Extended Data Fig. 2b), although to a different extent over time. In fact, pairing wild-type and 3×TgAD mice at these two times indicated a marked attenuation

[1]Laboratory for Integrative and Systems Physiology, Institute of Bioengineering, Ecole Polytechnique Fédérale de Lausanne, CH-1015 Lausanne, Switzerland. [2]Department of Translational Science and Molecular Medicine, Department of Family Medicine, Michigan State University, Grand Rapids, Michigan 49503, USA. [3]Proteomics Core Facility, Ecole Polytechnique Fédérale de Lausanne, CH-1015 Lausanne, Switzerland.
*These authors contributed equally to this work.

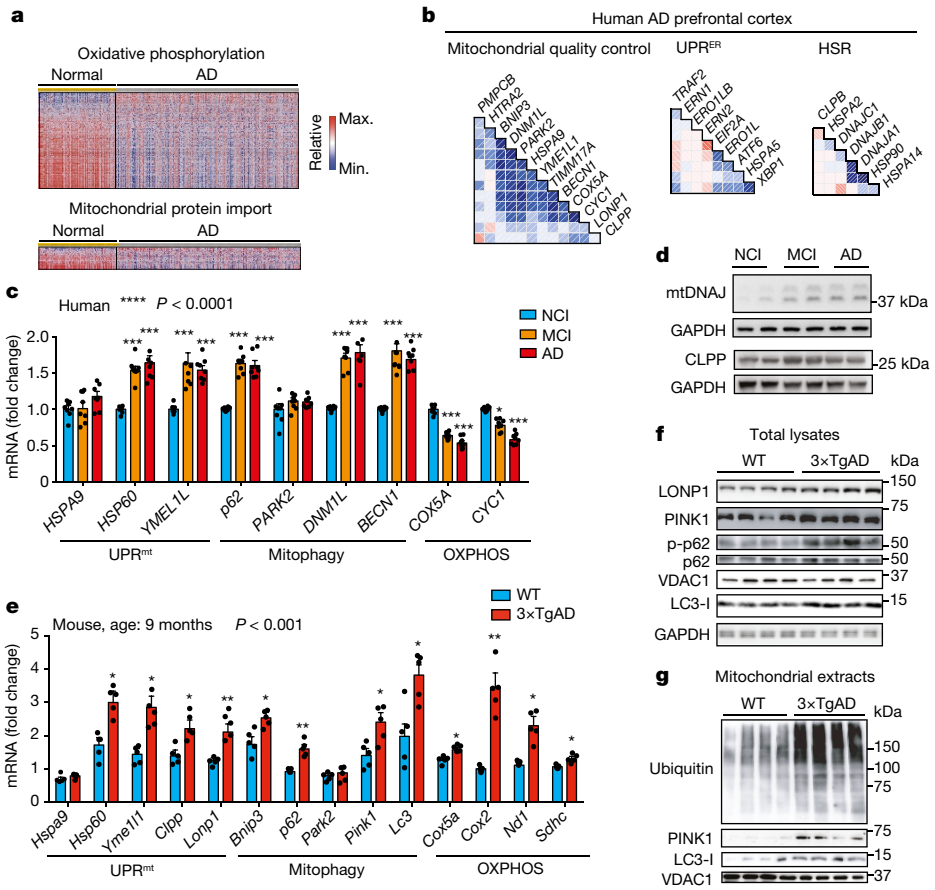

Figure 1 | Mitochondrial dysfunction in AD is typified by a conserved MSR. a, Heat map of the expression levels of OXPHOS and mitochondrial import genes in human prefrontal cortex of patients with AD (GN328; healthy, $n = 195$; AD, $n = 388$ individuals). **b**, Correlation plots of mitochondrial stress genes, UPR^{ER} and HSR levels in prefrontal cortex from patients with AD (GN328; n as in **a**). *PARK2* is also known as *PRKN*. See Extended Data Fig. 1 and Supplementary Table 1–5. **c**, **d**, Transcript analysis of the MSR signature (**c**; $n = 8$ per group) and western blot (**d**, $n = 2$ individuals) of mtDNAJ and CLPP in brains of humans with no cognitive impairment (NCI), mild-cognitive impairment (MCI) and mild to moderate AD. **e**, **f**, Transcript (**e**) and immunoblot (**f**) analysis of MSR gene and protein expression in the cortex of nine-month-old wild-type (WT) and 3×TgAD mice (wild-type, $n = 5$; 3×TgAD, $n = 5$ for RNA analysis; wild-type, $n = 4$; 3×TgAD, $n = 4$ for western blot analysis, representative of six animals). *Hsp60* is also known *Hspd1*; *p62* is also known as *Sqstm1*; *LC3* is also known as *Map1lc3a*; *Cox2* is also known as *mt-Co2*; *Nd1* is also known as *mt-Nd1*. **g**, Immunoblot (wild-type, $n = 4$; 3×TgAD, $n = 4$, representative of five animals) of mitophagy and autophagy proteins in mitochondrial extracts from cortex tissues of the mice in **e**, **f**. Data are mean ± s.e.m. $*P < 0.05$; $**P \leq 0.01$; $***P \leq 0.001$. Overall differences between conditions were assessed by two-way ANOVA. Differences in individual genes or proteins were assessed using two-tailed *t*-tests (95% confidence interval). All experiments were independently performed twice. See also Extended Data Fig. 2. For uncropped gel source data, see Supplementary Fig. 1. For all individual *P* values, see Source Data.

of this stress signature during disease progression (Extended Data Fig. 2d–f). Immunoblotting of total lysates from the cortex of wild-type and 3×TgAD mice showed the induction of PINK1, LONP1 and LC3 at both time points (Fig. 1f and Extended Data Fig. 2c). Additional analysis of the nine-month-old mice also indicated a reduction in VDAC, a marked increase in p62 phosphorylation (Fig. 1g) and reduced citrate synthase activity (Extended Data Fig. 2g) in mice with AD, indicative of autophagy and mitophagy. PINK1 and LC3-I, the unmodified form of LC3, were also increased in mitochondrial extracts from cortex samples of mice with AD (Fig. 1g), confirming that these proteins are recruited to the mitochondria to promote mitophagy, as supported by the increased ubiquitylation of mitochondrial proteins (Fig. 1g). For simplicity, we abbreviate the comprehensive mitochondrial stress footprint that we analysed as mitochondrial stress response (MSR).

Identification of a cross-species MSR signature

The functional impact of changes in mitochondrial homeostasis during disease and ageing in mammals can be modelled reliably using the nematode *C. elegans*[12]. Worm models of Aβ aggregation have been used extensively to study the basic consequences of proteotoxic stress on conserved biological pathways between worms and mammals[13,14]. We took advantage of the GMC101 worm model of Aβ proteotoxicity[15]. GMC101 worms constantly express the human Aβ isoform 1–42 in muscle cells, but adults only develop age-progressive paralysis and amyloid deposition in the body wall muscle after a temperature shift from 20 to 25 °C (ref. 15), whereas the control strain CL2122 does not express the Aβ peptide (Extended Data Fig. 3a).

Transcripts of the worm orthologues of MSR were induced in adult GMC101 worms compared to CL2122 after the temperature shift to 25 °C (Fig. 2a), whereas these were only partially changed at 20 °C (Extended Data Fig. 3b). The basal and maximal respiratory capacity were decreased in GMC101 worms (Fig. 2b and Extended Data Fig. 3c), in contrast to the increased OXPHOS transcript levels (Fig. 2a), suggesting a compensatory induction to ensure respiration. Mitochondrial content was lower in GMC101 worms, as shown by decreased OXPHOS proteins, a reduced mitochondrial:nuclear DNA ratio and decreased citrate synthase activity (Fig. 2c and Extended Data Fig. 3d, e). Notably, GMC101 fitness, measured as spontaneous movement[16], was robustly reduced relative to CL2122 worms in line with the muscle disorganization and alteration of the mitochondrial

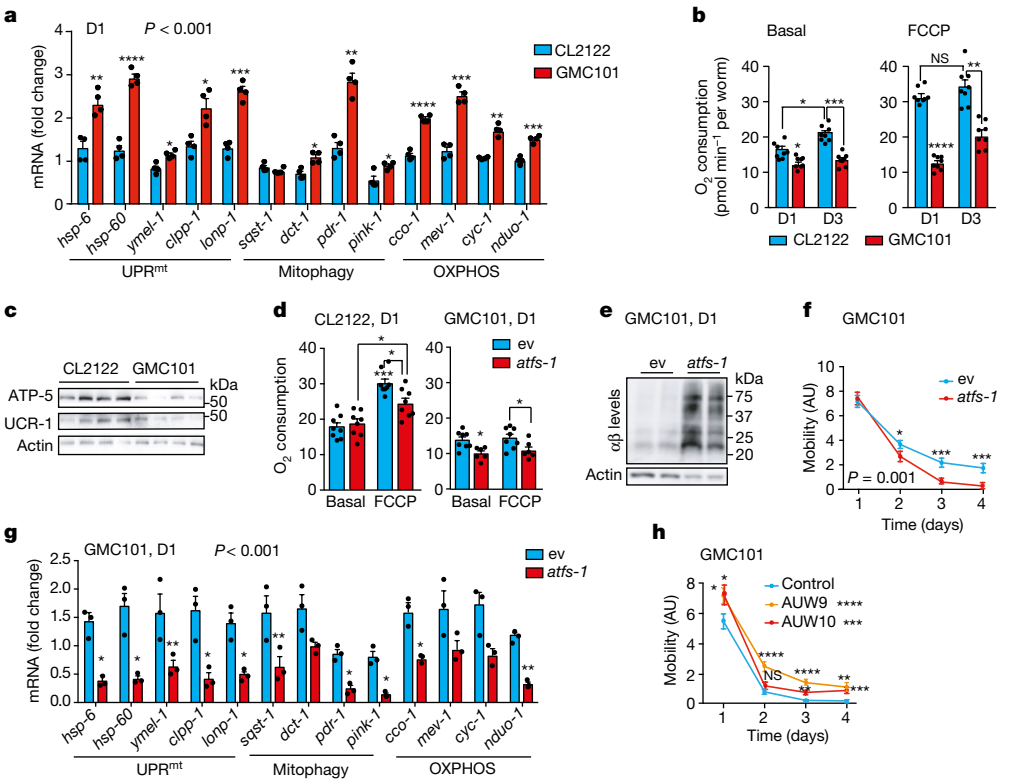

Figure 2 | Mitochondrial dysfunction and reliance on *atfs-1* in GMC101 worms after proteotoxic stress. a, MSR transcript analysis of day 1 (D1) CL2122 and GMC101 worms ($n = 3$ biologically independent samples). **b**, Basal respiration and after carbonyl cyanide-4-(trifluoromethoxy) phenylhydrazone (FCCP) (45 min, 10 μM) of day 1 (D1) and 3 (D3) adult worms (CL2122, $n = 8$; GMC101, $n = 8$ biologically independent samples). **c**, Immunoblot (CL2122, $n = 4$; GMC101, $n = 4$, representative of five biological replicates) of OXPHOS proteins in control and GMC101 at D1. **d**, Respiration assay as in **b** in CL2122 worms (ev, $n = 8$; *atfs-1*, $n = 8$ biologically independent samples) and GMC101 worms (ev, $n = 8$; *atfs-1*, $n = 6$ biologically independent samples) fed with *atfs-1* RNAi. **e**, Amyloid aggregation in GMC101 worms upon *atfs-1* RNAi shown by western blotting of two biological repeats. **f**, Mobility of GMC101 fed with 50% dilution of *atfs-1* RNAi (ev, $n = 59$; *atfs-1* 1/2, $n = 50$ worms). **g**, MSR transcript analysis of GMC101 worms upon *atfs-1* RNAi ($n = 3$ biologically independent samples). **h**, Mobility of control and *afts-1*-overexpressing GMC101 strains (GMC101, $n = 61$; AUW9, $n = 48$; AUW10, $n = 41$ worms). Data are mean ± s.e.m. $^*P < 0.05$; $^{**}P \leq 0.01$; $^{***}P \leq 0.001$; $^{****}P \leq 0.0001$; NS, not significant. Overall differences between conditions were assessed by two-way ANOVA. Differences in individual genes or proteins were assessed using two-tailed *t*-tests (95% confidence interval). All experiments were performed independently at least twice. ev, scrambled RNAi; AU, arbitrary units. See also Extended Data Figs 3–4. For uncropped gel source data, see Supplementary Fig. 1. For all individual *P* values, see Source Data.

network in the body wall muscle (Extended Data Fig. 3f, g). These data highlight the cross-species conservation of MSR, and show that GMC101 is an excellent proxy for the characterization of the mitochondrial dysfunction and phenotypic impact observed in Aβ diseases in mammals.

Mitochondrial homeostasis counteracts Aβ proteotoxicity

The control of mitochondrial function and UPR^{mt} during stress in the worm is mostly attributable to the activating transcription factor associated with stress, *atfs-1* (refs 17, 18). Depletion of *atfs-1* by RNA interference (RNAi) through feeding of GMC101, but not CL2122, worms, caused a severe developmental delay even in the absence of the disease-inducing temperature shift (Extended Data Fig. 3h), phenocopying mitochondrial respiration mutants that rely on *atfs-1* for survival and adaption[18]. Comparative analysis of transcripts involved in cytosolic and nuclear adaptation pathways, such as UPR^{ER}, HSR and *daf-16*, also showed a mild induction of the UPR^{ER} and a notable upregulation of the HSR in GMC101 worms (Extended Data Fig. 3i), in line with the role of the HSR as a primary defence against proteotoxic stress in worms[19]. We therefore evaluated the effect of RNAis targeting key regulators of these pathways, *hsf-1* and *xbp-1*, on the development of GMC101 worms. Only *atfs-1* RNAi led to extreme developmental delays in GMC101 worms, whereas no alterations were observed with any of these RNAis in CL2122 worms (Extended Data Fig. 3j).

Notably, basal and maximal respiration in adult GMC101 worms was significantly impaired upon *atfs-1* silencing, whereas only the maximal respiration was partially affected in CL2122 worms (Fig. 2d). In addition, *atfs-1* RNAi exacerbated aggregation (Fig. 2e and Extended Data Fig. 3k) and paralysis (Fig. 2f) in GMC101 worms, whereas the mobility of CL2122 worms was unaffected (Extended Data Fig. 3l). Furthermore, *atfs-1* knockdown in GMC101 worms prominently repressed the MSR signature, including mitophagy effectors (Fig. 2g), whereas in CL2122 worms, *pdr-1*, *dct-1* and OXPHOS transcripts were even induced, despite silencing of *atfs-1* in both strains (Extended Data Fig. 3m, n).

Given the induction of the HSR in GMC101 worms, we tested whether *hsf-1* repression would have an effect on fitness. Notably, while *atfs-1* knockdown paralysed only GMC101 worms, silencing of *hsf-1* reduced mobility in both CL2122 and wild-type N2 strains when incubated at 25 °C (Extended Data Fig. 3o), reflecting a general effect of *hsf-1* on homeostasis independent of the strain. Worm mobility was similarly impaired in GMC101, but not in CL2122, worms following silencing of *atfs-1* with an alternative RNAi that we generated (*atfs-1* #2) (Extended Data Fig. 3p, q and Supplementary Table 13), confirming a specific role of *atfs-1* in ensuring organismal homeostasis in GMC101 worms. Furthermore, silencing of *ubl-5*, another positive regulator of the UPR^{mt} (ref. 20), also delayed development and decreased health- and lifespan specifically in GMC101 worms (Extended Data Fig. 4a–c). Interestingly, *atfs-1* silencing led to further upregulation of the HSR in GMC101 worms and to its induction in CL2122 worms (Extended Data

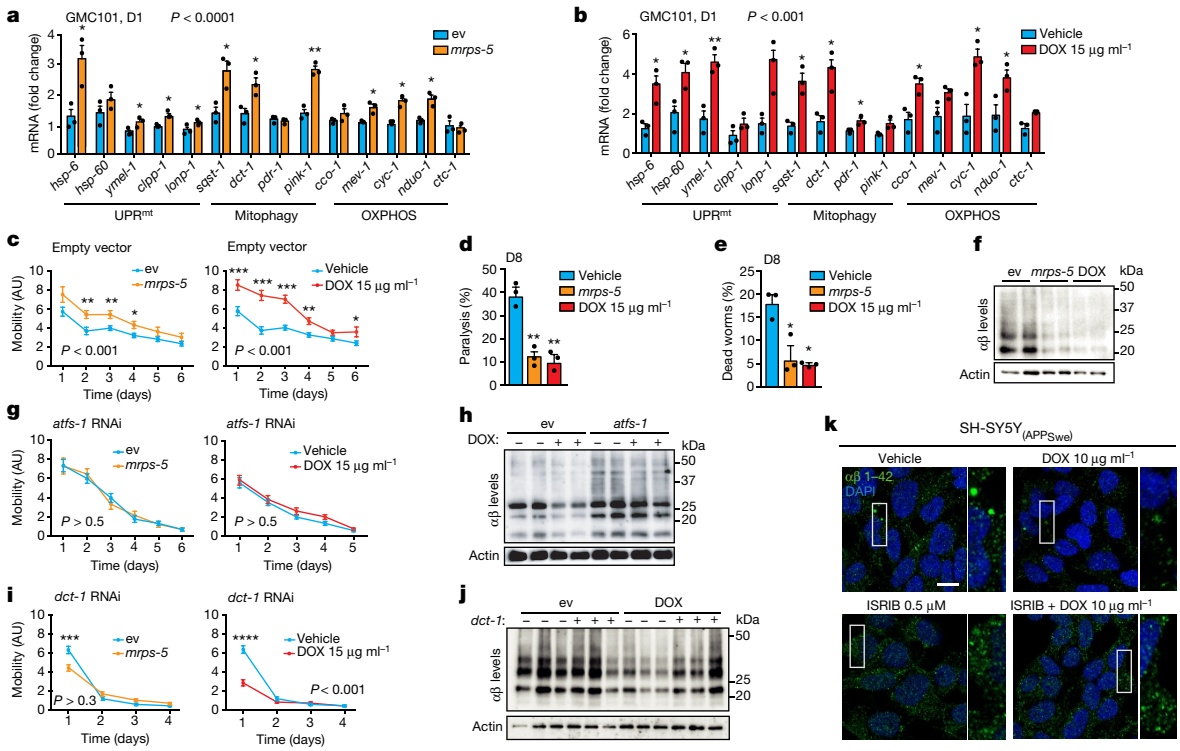

Figure 3 | Inhibiting mitochondrial translation reduces Aβ proteotoxicity and aggregation in GMC101 worms and in cells. **a**, **b**, MSR transcript levels in GMC101 worms that were fed *mrps-5* RNAi or treated with DOX (**a**, **b**, $n = 3$ biologically independent samples). **c**, Mobility of GMC101 upon *mrps-5* RNAi ($n = 35$ worms) or DOX treatment ($n = 54$ worms). The ANOVA *P* values are reported on the left bottom side of the plots. **d**, **e**, Percentage of paralysed (**d**) and dead (**e**) D8 adult GMC101 worms after *mrps-5* RNAi or DOX treatment ($n = 3$ independent experiments). **f**, Western blot of amyloid aggregation in GMC101 upon *mrps-5* RNAi or DOX treatment ($n = 2$ biologically independent samples). **g**, Mobility of GMC101 worms upon *atfs-1* RNAi feeding (ev, $n = 54$; *mrps-5*, $n = 49$; DOX, $n = 49$ worms). The ANOVA *P* values are reported on the left bottom side of the plots. **h**, Amyloid aggregation in DOX-treated GMC101 worms upon *atfs-1* RNAi ($n = 2$ biological replicates). **i**, Mobility of GMC101 upon *dct-1* RNAi (ev, $n = 44$; DOX, $n = 59$; *mrps-5*, $n = 66$ worms). $^{***}P = 0.0004$; $^{****}P \leq 0.0001$. The ANOVA *P* values are reported on the bottom of the plots. **j**, Amyloid aggregation in DOX-treated GMC101 worms upon *dct-1* RNAi ($n = 3$ biologically independent samples). **k**, Confocal images of the SH-SY5Y neuroblastoma cell line stained with the anti-β-amyloid 1–42 antibody, after DOX and, where indicated, ISRIB treatments for 24 h. Scale bar, 10 µm. See Methods for further details. Data are mean ± s.e.m. $^{*}P < 0.05$; $^{**}P \leq 0.01$; $^{***}P \leq 0.001$; $^{****}P \leq 0.0001$. Overall differences between conditions were assessed by two-way ANOVA. Differences in individual genes or between two groups were assessed using two-tailed *t*-tests (95% confidence interval). All experiments were performed independently at least twice. ev, scrambled RNAi; DOX, doxycycline; AU, arbitrary units; ISRIB, integrated stress response inhibitor. See also Extended Data Fig. 5. For uncropped gel source data, see Supplementary Fig. 1. For all individual *P* values, see Source Data.

Fig. 4d, e), while repressing the MSR specifically in GMC101 worms (Fig. 2g and Extended Data Fig. 3n).

Conversely, to increase *atfs-1* function, we generated two GMC101-derived strains, AUW9 and AUW10, and one CL2122-derived line (AUW11), overexpressing *atfs-1* (Supplementary Tables 12, 13). This resulted in induction of the UPR^{mt} (Extended Data Fig. 4f), a significant increase in fitness and a decrease in paralysis and death scores in the GMC101-derived strains AUW9 and AUW10 (Fig. 2h and Extended Data Fig. 4g, h), while no changes were observed in AUW11 worms (Extended Data Fig. 4g). As an alternative approach to increase the MSR, we crossed GMC101 worms with two long-lived mitochondrial mutants, that is, *clk-1* (ref. 21) and *nuo-6* (ref. 22) (Supplementary Tables 12, 13). Consistently, GMC101 worms with a mutation in these mitochondrial genes (AUW12, with the *clk-1* mutation, and AUW13, mutated for *nuo-6*) had intermediate phenotypes between GMC101 and the mitochondrial mutants, with an increased health- and lifespan (Extended Data Fig. 4i–l).

Together, these results indicate that *atfs-1* and the induction of MSR ensure proteostasis and survival in this worm model of Aβ aggregation, and that mitochondria have an active, rather than passive, role during Aβ proteotoxic stress. This prompted us to investigate the potential of increasing mitochondrial proteostasis to halt the progression of this deleterious phenotype.

Effect of mitochondrial translation on Aβ proteotoxicity

Given the strong association between UPR^{mt} and AD observed above, we investigated the effects of two established strategies to induce UPR^{mt} in *C. elegans*: genetically, by silencing the expression of the mitochondrial ribosomal protein *mrps-5* (ref. 23); and pharmacologically, by using the mitochondrial translation inhibitor doxycycline (DOX)[23,24]. Both interventions, which increase worm health and lifespan[23], markedly induced transcripts of UPR^{mt}, mitophagy and respiration genes in GMC101 worms (Fig. 3a, b), without causing major development and growth delays (Extended Data Fig. 5a). DOX similarly induced these pathways in CL2122 worms (Extended Data Fig. 5b). No changes in UPR^{ER} and HSR were observed in GMC101 worms treated with DOX or *mrps-5* RNAi (Extended Data Fig. 5c, d), whereas one *daf-16* target, the mitochondrial superoxide dismutase *sod-3*, was induced (Extended Data Fig. 5c, d). The transcriptional induction of the MSR positively affected fitness and lifespan of GMC101 worms (Fig. 3c–e). Furthermore, Aβ aggregation was reduced by *mrps-5* RNAi and DOX (Fig. 3f and Extended Data Fig. 5e). Importantly, the improvement in motility and Aβ clearance in GMC101 worms required *atfs-1* (Fig. 3g, h), demonstrating the contribution of the UPR^{mt} to the phenotypic improvements. Respirometry on GMC101 worms fed with *mrps-5* RNAi at day 3 and day 6 of adulthood (Extended Data Fig. 5f), showed that *mrps-5* knockdown prevented the decrease in respiration upon

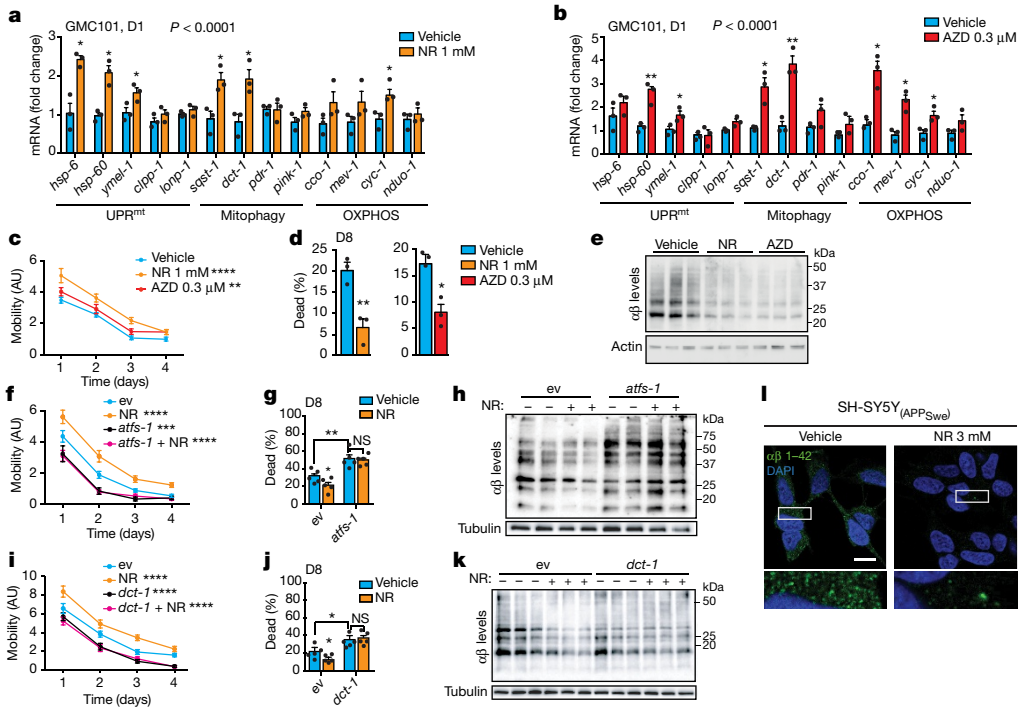

Figure 4 | NAD$^+$ boosters reduce Aβ proteotoxicity and aggregation in GMC101 worms and cells. a, **b**, MSR transcripts in GMC101 worms treated with NR (**a**) or AZD (**b**) (**a**, **b**, $n = 3$ biologically independent samples). **c**, Mobility of GMC101 worms treated with NR ($n = 50$ worms) or AZD ($n = 39$ worms). $^{**}P \leq 0.001$ (AZD, $P = 0.006$); $^{****}P \leq 0.0001$ (NR). **d**, Percentage of dead D8 adult GMC101 worms after NR or AZD treatment ($n = 3$ independent experiments). **e**, Western blot of amyloid aggregation in GMC101 worms after NR or AZD treatment ($n = 3$ biologically independent samples for all groups). **f**, Mobility of GMC101 worms treated with NR upon *atfs-1* RNAi feeding (ev, $n = 52$; *atfs-1*, $n = 38$; NR, $n = 40$; NR, *atfs-1*, $n = 41$ worms). $^{***}P \leq 0.001$ (*atfs-1*, $P = 0.0006$). **g**, Percentage of dead D8 adult GMC101 worms treated with NR upon *atfs-1* RNAi ($n = 5$ biologically independent samples). **h**, Amyloid aggregation in NR-treated GMC101 worms upon *atfs-1* RNAi feeding (western blot, representative of two biological replicates). **i**, Mobility of NR-treated GMC101 worms upon *dct-1* RNAi (ev, $n = 41$; *dct-1*, $n = 40$; NR, $n = 39$; NR, *dct-1*, $n = 50$ worms). **j**, Percentage of dead D8 adult GMC101 worms treated with NR upon *dct-1* RNAi ($n = 5$ biologically independent samples). **k**, Amyloid aggregation immunoblot in NR-treated GMC101 worms upon *dct-1* RNAi ($n = 3$ biologically independent samples). **l**, Confocal images of APPSwe SH-SY5Y cells stained with anti-β-amyloid 1–42 antibody, after 24 h of NR treatment. Scale bar, 10 µm. Data are mean ± s.e.m. $^{*}P < 0.05$; $^{**}P \leq 0.01$; $^{***}P \leq 0.001$; $^{****}P \leq 0.0001$; NS, not significant. Overall differences between conditions were assessed by two-way ANOVA. Differences in individual genes or between two groups were assessed using two-tailed *t*-tests (95% confidence interval). All experiments were performed independently at least twice. ev, scrambled RNAi; AU, arbitrary units. See also Extended Data Fig. 6. For uncropped gel source data, see Supplementary Fig. 1. For all individual *P* values, see Source Data.

ageing, suggesting a stabilization of mitochondrial function following the MSR-dependent improvement of proteostasis.

We then extended our investigation to a human SH-SY5Y neuroblastoma cell line expressing the Swedish K670N/M671L mutation in APP (APP_{Swe})[25]. DOX markedly reduced intracellular Aβ deposits, as shown with an Aβ1–42-specific antibody (Fig. 3k and Extended Data Fig. 5g). This improvement was linked to a mitochondrial–nuclear protein imbalance and the induction of components of the MSR (Extended Data Fig. 5h, i). These results add to observations of *in vitro*[26] and *in vivo* studies in flies[27] and patients[28] with AD, which have suggested that DOX treatment may ameliorate AD and Aβ aggregation. Recently, the regulation of the mitochondrial stress responses in mammals, including DOX-dependent mitochondrial stress, was shown to rely on the activation of the integrated stress response (ISR) and on the transcription factor ATF4 (refs 29–31). Pretreating cells with ISRIB, a global ISR inhibitor[32], prevented amyloid clearance by DOX and interfered with DOX-mediated induction of canonical ATF4 target genes, such as *CHOP* and *CHAC1* (ref. 29) (Fig. 3k and Extended Data Fig. 5g, j). This suggests that ISR is involved in resolving Aβ proteotoxic stress in mammalian cells.

Given the induction of mitophagy in 3×TgAD mice, human patients with AD and in GMC101 worms, and its further increase upon *mrps-5* RNAi and DOX treatments, we also tested the contribution of mitophagy to the homeostasis of GMC101 worms. To achieve this, we silenced, using RNAi, *dct-1*, an evolutionarily conserved regulator of mitophagy[33]. *dct-1* RNAi already reduced the health- and lifespan of GMC101 worms in basal conditions (Extended Data Fig. 5k–m). Furthermore, it decreased the positive effects of *mrps-5* RNAi and DOX on health- and lifespan (Fig. 3i and Extended Data Fig. 5l, m) and proteostasis (Fig. 3j). Conversely, *dct-1* knockdown in CL2122 worms affected their movement only during ageing (Extended Data Fig. 5n, o), stressing the relevance of mitophagy in ageing. Taken together, these data show that mitophagy, in addition to UPR^{mt}, is induced and required for the survival of GMC101 worms and for the beneficial effects of the described interventions.

NAD$^+$ boosters attenuate Aβ proteotoxicity

The UPR^{mt} and mitophagy pathways are also potently induced in worms and in various mammalian tissues by NAD$^+$-boosting compounds, such as nicotinamide riboside (NR) and Olaparib (AZD2281 or AZD)[34–37]. Similar to DOX treatment and *mrps-5* RNAi, treatment of GMC101 worms with NR and AZD induced MSR (Fig. 4a, b), and improved health- and lifespan (Fig. 4c, d and Extended Data Fig. 6a). The NR- and AZD-mediated induction of the MSR was also observed in CL2122 worms (Extended Data Fig. 6b, c); however, these treatments only improved CL2122 fitness during ageing (Extended Data Fig. 6d, e), similar to what has previously been shown in N2 worms[34]. In addition, treatment of GMC101 worms with NR and AZD reduced proteotoxic stress (Fig. 4e). Notably, the NR-mediated phenotypic and proteostasis benefits required *atfs-1* (Fig. 4f–h and Extended Data Fig. 6f) and *dct-1*

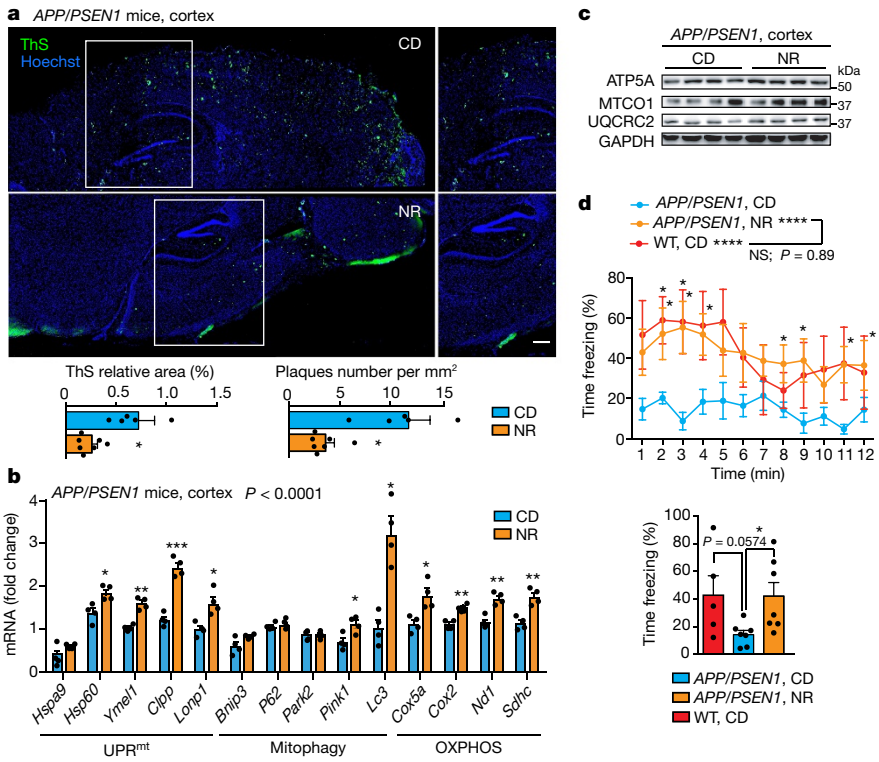

Figure 5 | NR reduces Aβ deposits, induces the MSR and improves contextual memory in transgenic mice with AD. a, Representative images and corresponding quantification of plaques in cortex samples of $APP_{Swe}/PSEN1_{dE9}$ mice (*APP/PSEN1*) with AD following NR treatment, stained using thioflavin S (ThS) (chow diet, $n = 5$ mice; NR, $n = 7$ mice; NR treatment: 400 mg kg^{-1} per day for 10 weeks). Scale bar, 200 μm. $^{*}P < 0.05$ (relative area, $P = 0.041$; number, $P = 0.014$). **b**, **c**, MSR transcript (**b**) and immunoblot (**c**) analyses of cortex samples of $APP_{Swe}/PSEN1_{dE9}$ mice following NR treatment (**b**, $n = 5$ animals per group; **c**, $n = 4$ animals per group). Data are representative of two independent experiments. **d**, Contextual fear conditioning in wild-type ($n = 5$ mice) and $APP_{Swe}/PSEN1_{dE9}$ ($n = 7$ mice) mice with or without NR treatment, plotted as a function of the time interval (left) or as an average of the total obtained values (right). $^{*}P < 0.05$ ($P = 0.03$); $^{****}P \leq 0.0001$. One-tail *t*-test performed between averaged values of wild-type and $APP_{Swe}/PSEN1_{dE9}$ mice ($P = 0.0574$, 95% confidence interval). Data are mean ± s.e.m. $^{*}P < 0.05$; $^{**}P \leq 0.01$; $^{***}P \leq 0.001$; $^{****}P \leq 0.0001$; NS, not significant. Overall differences between conditions were assessed by two-way ANOVA, unless indicated. Differences in individual genes or between two groups were assessed using two-tailed *t*-tests (95% confidence interval). See Methods for further details. CD, chow diet. For uncropped gel source data, see Supplementary Fig. 1. For all individual *P* values, see Source Data.

(Fig. 4i–k and Extended Data Fig. 6g). NR has been shown to increase sirtuin activity and activate FOXO (encoded by *daf-16* in *C. elegans*) signalling in mammals and *C. elegans*[34]. Therefore, we evaluated the effect of *daf-16* and *sir-2.1* silencing on development, healthspan and NR-dependent benefits in GMC101 worms. Whereas *sir-2.1* knockdown did not delay growth of GMC101 or control CL2122 worms (Extended Data Fig. 6h), it increased paralysis and death in GMC101 worms similar to what was found in GMC101 worms treated with *dct-1* and *atfs-1* RNAi clones (Extended Data Fig. 6i, k). However, NR still significantly rescued health- and lifespan of GMC101 worms fed with *sir-2.1* RNAi, showing that the effects of NR rely mostly on *atfs-1* and *dct-1* (Extended Data Fig. 6i, k). Instead, feeding GMC101 worms with *daf-16* RNAi did not result in major phenotypic changes (Extended Data Fig. 6h, j, k). Furthermore, NR did not affect the expression of *daf-16* and its targets (Extended Data Fig. 6l). NR and AZD had only a minimal impact on UPR^{ER} and HSR in GMC101 worms, with the induction of *hsp-16.41*, *hsp-16.48* and *hsp-16.49* (*hsp-16.48/49)* (Extended Data Fig. 6l, m). These results indicate that in the GMC101 model, the main mode of action of NAD^{+} boosting involves the induction of the MSR.

We also assessed the effect of NR on human Aβ-expressing neuroblastoma cells and, consistent with the data from the *C. elegans* model, we observed a remarkable reduction in intracellular Aβ deposits with NR (Fig. 4l and Extended Data Fig. 6n), accompanied by increased OXPHOS protein (Extended Data Fig. 5h) and MSR transcript levels (Extended Data Fig. 6o).

NR reduces Aβ levels in transgenic mice with AD

We have previously shown that NR exerts beneficial effects on health- and lifespan[34,36], but whether it also improves mitochondrial function and proteostasis *in vivo* in a mouse model of Aβ proteotoxicity remains unknown. We therefore treated $APP_{Swe}/PSEN1_{dE9}$ mice with AD with NR and assessed the levels of Aβ plaques in brain using thioflavin S, as well as mitochondrial OXPHOS and MSR transcript and protein expression. Consistent with the effects observed in cells and worms, NR robustly reduced Aβ deposits in cortex tissues of the mice with AD (Fig. 5a), and induced the MSR mRNA signature (Fig. 5b) and OXPHOS protein levels (Fig. 5c). NR also increased context-dependent memory in the $APP_{Swe}/PSEN1_{dE9}$ mice with AD, which was impaired compared to wild-type mice, as assessed by contextual fear conditioning[38] (Fig. 5d), suggesting a potential positive impact on cognitive function. We therefore propose that restoring or increasing mitochondrial function and proteostasis induces a conserved repair mechanism, in worms and mice, that leads to decreased Aβ proteotoxicity and improves health- and lifespan.

Discussion

Proteotoxic stress in Aβ diseases, such as AD, is associated with mitochondrial dysfunction, and reduced OXPHOS activity has been considered one of the major hallmarks of these diseases. Here, we identify a cross-species mitochondrial stress response signature that implicates mitochondrial proteostasis as a key mechanism in response to Aβ proteotoxic stress. Notably, we show that Aβ accumulation induces both UPR^{mt} and mitophagy in a manner that is conserved from *C. elegans* to humans. Currently, the molecular mechanism driving this induction is still unclear. On the basis of our results, we speculate that it involves the alteration of a basic, conserved functional process, such as mitochondrial import, which is linked to the activation of the UPR^{mt} (ref. 18), is disrupted during Aβ proteotoxic stress[39] and is downregulated in patients with AD in our analyses. Our work also provides evidence that mitochondria have an active role in the pathogenesis of Aβ diseases, as reducing mitochondrial homeostasis via *atfs-1* depletion in GMC101 worms aggravates the hallmarks of the disease (model in Extended Data Fig. 7); conversely, boosting mitochondrial proteostasis by increasing the UPR^{mt} and mitophagy decreases protein aggregation, restores worm fitness and delays disease progression, ultimately translating to increased lifespan. Similarly, in mammals we show that DOX and NR decrease Aβ accumulation in a human SH-SY5Y neuronal cell line and that NR treatment reduces amyloid plaque formation in the brain and improves contextual memory in $APP_{Swe}/PSEN1_{dE9}$ mice with AD. These findings indicate that boosting mitochondrial function and proteostasis may decrease the formation of detrimental protein aggregates in the context of proteotoxic diseases, which are characterized by reduced mitochondrial activity and loss of proteostasis. Together with

initial evidence suggesting potential benefits of targeting dysfunctional mitochondria in AD[26–28,40,41] and in view of recent findings linking mitochondrial stress to the induction of cytosolic proteostasis mechanisms[42–45], our data support the concept that increasing mitochondrial proteostasis may have potential for the management of pervasive Aβ proteopathies, such as AD.

Online Content Methods, along with any additional Extended Data display items and Source Data, are available in the online version of the paper; references unique to these sections appear only in the online paper.

Received 12 January; accepted 17 November 2017.
Published online 6 December 2017.

1. Alzheimer's Association. 2016 Alzheimer's disease facts and figures. *Alzheimers Dement.* **12,** 459–509 (2016).
2. Dember, L. M. Amyloidosis-associated kidney disease. *J. Am. Soc. Nephrol.* **17,** 3458–3471 (2006).
3. Askanas, V. & Engel, W. K. Sporadic inclusion-body myositis: conformational multifactorial ageing-related degenerative muscle disease associated with proteasomal and lysosomal inhibition, endoplasmic reticulum stress, and accumulation of amyloid-β42 oligomers and phosphorylated tau. *Presse Med.* **40,** e219–e235 (2011).
4. Gauthier, S. *et al.* Why has therapy development for dementia failed in the last two decades? *Alzheimers Dement.* **12,** 60–64 (2016).
5. Soejitno, A., Tjan, A. & Purwata, T. E. Alzheimer's disease: lessons learned from amyloidocentric clinical trials. *CNS Drugs* **29,** 487–502 (2015).
6. Herrup, K. *et al.* Beyond amyloid: getting real about non-amyloid targets in Alzheimer's disease. *Alzheimers Dement.* **9,** 452–458 (2013).
7. Selfridge, J. E., E, L., Lu, J. & Swerdlow, R. H. Role of mitochondrial homeostasis and dynamics in Alzheimer's disease. *Neurobiol. Dis.* **51,** 3–12 (2013).
8. Pellegrino, M. W. & Haynes, C. M. Mitophagy and the mitochondrial unfolded protein response in neurodegeneration and bacterial infection. *BMC Biol.* **13,** 22 (2015).
9. Beck, J. S., Mufson, E. J. & Counts, S. E. Evidence for mitochondrial UPR gene activation in familial and sporadic Alzheimer's disease. *Curr. Alzheimer Res.* **13,** 610–614 (2016).
10. Mufson, E. J. *et al.* Mild cognitive impairment: pathology and mechanisms. *Acta Neuropathol.* **123,** 13–30 (2012).
11. Oddo, S. *et al.* Triple-transgenic model of Alzheimer's disease with plaques and tangles: intracellular Aβ and synaptic dysfunction. *Neuron* **39,** 409–421 (2003).
12. Jovaisaite, V., Mouchiroud, L. & Auwerx, J. The mitochondrial unfolded protein response, a conserved stress response pathway with implications in health and disease. *J. Exp. Biol.* **217,** 137–143 (2014).
13. Cohen, E., Bieschke, J., Perciavalle, R. M., Kelly, J. W. & Dillin, A. Opposing activities protect against age-onset proteotoxicity. *Science* **313,** 1604–1610 (2006).
14. Link, C. D. *C. elegans* models of age-associated neurodegenerative diseases: lessons from transgenic worm models of Alzheimer's disease. *Exp. Gerontol.* **41,** 1007–1013 (2006).
15. McColl, G. *et al.* Utility of an improved model of amyloid-beta ($A\beta_{1-42}$) toxicity in *Caenorhabditis elegans* for drug screening for Alzheimer's disease. *Mol. Neurodegener.* **7,** 57 (2012).
16. Mouchiroud, L. *et al.* The movement tracker: a flexible system for automated movement analysis in invertebrate model organisms. *Curr. Protoc. Neurosci.* **77,** 8.37.1–8.37.21 (2016).
17. Nargund, A. M., Fiorese, C. J., Pellegrino, M. W., Deng, P. & Haynes, C. M. Mitochondrial and nuclear accumulation of the transcription factor ATFS-1 promotes OXPHOS recovery during the UPR^{mt}. *Mol. Cell* **58,** 123–133 (2015).
18. Nargund, A. M., Pellegrino, M. W., Fiorese, C. J., Baker, B. M. & Haynes, C. M. Mitochondrial import efficiency of ATFS-1 regulates mitochondrial UPR activation. *Science* **337,** 587–590 (2012).
19. Prahlad, V. & Morimoto, R. I. Integrating the stress response: lessons for neurodegenerative diseases from *C. elegans*. *Trends Cell Biol.* **19,** 52–61 (2009).
20. Benedetti, C., Haynes, C. M., Yang, Y., Harding, H. P. & Ron, D. Ubiquitin-like protein 5 positively regulates chaperone gene expression in the mitochondrial unfolded protein response. *Genetics* **174,** 229–239 (2006).
21. Wong, A., Boutis, P. & Hekimi, S. Mutations in the *clk-1* gene of *Caenorhabditis elegans* affect developmental and behavioral timing. *Genetics* **139,** 1247–1259 (1995).
22. Yang, W. & Hekimi, S. Two modes of mitochondrial dysfunction lead independently to lifespan extension in *Caenorhabditis elegans*. *Aging Cell* **9,** 433–447 (2010).
23. Houtkooper, R. H. *et al.* Mitonuclear protein imbalance as a conserved longevity mechanism. *Nature* **497,** 451–457 (2013).
24. Moullan, N. *et al.* Tetracyclines disturb mitochondrial function across eukaryotic models: a call for caution in biomedical research. *Cell Rep.* **10,** 1681–1691 (2015).
25. Zheng, L. *et al.* Macroautophagy-generated increase of lysosomal amyloid β-protein mediates oxidant-induced apoptosis of cultured neuroblastoma cells. *Autophagy* **7,** 1528–1545 (2011).
26. Forloni, G., Colombo, L., Girola, L., Tagliavini, F. & Salmona, M. Anti-amyloidogenic activity of tetracyclines: studies *in vitro*. *FEBS Lett.* **487,** 404–407 (2001).
27. Costa, R., Speretta, E., Crowther, D. C. & Cardoso, I. Testing the therapeutic potential of doxycycline in a *Drosophila melanogaster* model of Alzheimer disease. *J. Biol. Chem.* **286,** 41647–41655 (2011).
28. Loeb, M. B. *et al.* A randomized, controlled trial of doxycycline and rifampin for patients with Alzheimer's disease. *J. Am. Geriatr. Soc.* **52,** 381–387 (2004).
29. Quirós, P. M. *et al.* Multi-omics analysis identifies ATF4 as a key regulator of the mitochondrial stress response in mammals. *J. Cell Biol.* **216,** 2027–2045 (2017).
30. Münch, C. & Harper, J. W. Mitochondrial unfolded protein response controls matrix pre-RNA processing and translation. *Nature* **534,** 710–713 (2016).
31. Bao, X. R. *et al.* Mitochondrial dysfunction remodels one-carbon metabolism in human cells. *eLife* **5,** e10575 (2016).
32. Sidrauski, C., McGeachy, A. M., Ingolia, N. T. & Walter, P. The small molecule ISRIB reverses the effects of $eIF2\alpha$ phosphorylation on translation and stress granule assembly. *eLife* **4,** e05033 (2015).
33. Palikaras, K., Lionaki, E. & Tavernarakis, N. Coordination of mitophagy and mitochondrial biogenesis during ageing in *C. elegans*. *Nature* **521,** 525–528 (2015).
34. Mouchiroud, L. *et al.* The NAD^+/sirtuin pathway modulates longevity through activation of mitochondrial UPR and FOXO signaling. *Cell* **154,** 430–441 (2013).
35. Gariani, K. *et al.* Eliciting the mitochondrial unfolded protein response by nicotinamide adenine dinucleotide repletion reverses fatty liver disease in mice. *Hepatology* **63,** 1190–1204 (2016).
36. Zhang, H. *et al.* NAD^+ repletion improves mitochondrial and stem cell function and enhances life span in mice. *Science* **352,** 1436–1443 (2016).
37. Fang, E. F. *et al.* NAD^+ replenishment improves lifespan and healthspan in ataxia telangiectasia models via mitophagy and DNA repair. *Cell Metab.* **24,** 566–581 (2016).
38. Corcoran, K. A., Lu, Y., Turner, R. S. & Maren, S. Overexpression of *hAPPswe* impairs rewarded alternation and contextual fear conditioning in a transgenic mouse model of Alzheimer's disease. *Learn. Mem.* **9,** 243–252 (2002).
39. Cenini, G., Rüb, C., Bruderek, M. & Voos, W. Amyloid β-peptides interfere with mitochondrial preprotein import competence by a coaggregation process. *Mol. Biol. Cell* **27,** 3257–3272 (2016).
40. Gong, B. *et al.* Nicotinamide riboside restores cognition through an upregulation of proliferator-activated receptor-γ coactivator 1α regulated β-secretase 1 degradation and mitochondrial gene expression in Alzheimer's mouse models. *Neurobiol. Aging* **34,** 1581–1588 (2013).
41. Martire, S. *et al.* Bioenergetic impairment in animal and cellular models of Alzheimer's disease: PARP-1 inhibition rescues metabolic dysfunctions. *J. Alzheimers Dis.* **54,** 307–324 (2016).
42. Kim, H. E. *et al.* Lipid biosynthesis coordinates a mitochondrial-to-cytosolic stress response. *Cell* **166,** 1539–1552 (2016).
43. Wang, X. & Chen, X. J. A cytosolic network suppressing mitochondria-mediated proteostatic stress and cell death. *Nature* **524,** 481–484 (2015).
44. Wrobel, L. *et al.* Mistargeted mitochondrial proteins activate a proteostatic response in the cytosol. *Nature* **524,** 485–488 (2015).
45. D'Amico, D., Sorrentino, V. & Auwerx, J. Cytosolic proteostasis networks of the mitochondrial stress response. *Trends Biochem. Sci.* **42,** 712–725 (2017).

Supplementary Information is available in the online version of the paper.

Acknowledgements We thank P. Gönczy and M. Pierron (EPFL) for sharing reagents, the *Caenorhabditis* Genetics Center, which is funded by NIH Office of Research Infrastructure Programs (P40 OD010440), for providing worm strains. V.S. is supported by the 'EPFL Fellows' program co-funded by the Marie Skłodowska-Curie, Horizon 2020 Grant agreement (665667). D.D. is supported by a fellowship funded by Associazione Italiana per la Ricerca sul Cancro (AIRC). S.E.C. is supported by NIH grants (P01AG014449, R21AG053581 and P30 AG053760). The research of J.A. is supported by the EPFL, NIH (R01AG043930), Systems X (SySX.ch 2013/153), Velux Stiftung (1019), the Jebsen Foundation and the Swiss National Science Foundation (31003A-140780).

Author Contributions V.S. and J.A. conceived and designed the project. V.S., L.M., M.R., J.S.B., H.Z., D.D., F.P., N.M., A.W.S., S.R. and S.E.C. performed the experiments. V.S., M.R. and L.M. independently replicated worm experiments in Figs 2–4. V.S., L.M. and J.A. wrote the manuscript.

Author Information Reprints and permissions information is available at www.nature.com/reprints. The authors declare no competing financial interests. Readers are welcome to comment on the online version of the paper. Publisher's note: Springer Nature remains neutral with regard to jurisdictional claims in published maps and institutional affiliations. Correspondence and requests for materials should be addressed to J.A. (admin.auwerx@epfl.ch).

METHODS

Animal experiments. 3×TgAD male mice, bearing human mutant APP_{Swe}, PS1M146V and TauP301L transgenes[11], and wild-type, hybrid 129/C57BL/6 mouse littermates were transcardially perfused with saline at six and nine months of age ($n=6$ per group) and brains from each group were hemisected. One hemisphere was immersion-fixed in 4% paraformaldehyde and 0.1% glutaraldehyde for 24 h and stored in cryoprotectant. From the other hemisphere, the hippocampus, frontoparietal cortex and cerebellum were rapidly dissected and snap-frozen.

APP_{Swe}/$PSEN1_{dE9}$ male mice (Tg(APP_{Swe},PSEN1dE9)85Dbo/Mmjax) were purchased from JAX. *APP_{Swe}/$PSEN1_{dE9}$* mice were fed NR pellets (400 mg kg^{-1} per day) for 10 weeks, starting at the age of 4 months. The pellets were prepared by mixing powdered chow diet (2016S, Harlan Laboratories) with water or with NR dissolved in water. Pellets were dried under a laminar flow hood for 48 h. Mice were housed in groups of two to four animals per cage and randomized to 7–8 animals per experimental group according to their body weight. No blinding was used during the experiment procedures.

Fear conditioning. Fear conditioning was conducted as described previously[38], using chambers placed in sound-attenuating boxes (635 × 420 × 445 mm) (Med Associates). Each chamber is equipped with lights (infrared and visible), speakers and the floor of the chamber consisted of a stainless-steel grid connected to a shock generator. A computer running MED PC-IV (Med Associates) controls the presentation of the stimuli (tone and shock). A video camera connected to the MED-VFC-NIR-M automated video-tracking system was used to detect and record movements and freezing behaviour. On the first day (conditioning session), mice were habituated to the testing chamber for 2 min followed by the presentation of an auditory cue for 30 s (5 kHz tone; 80 dB, conditioned stimulus (CS)), co-terminating with a foot shock during the last 2 s (0.7 mA; unconditioned stimulus (US)). Mice received four CS–US pairings with an inter-trial interval of 2 min. The last CS–US pairing was followed by a 2-min resting phase before mice were returned to their home cage. The entire conditioning session lasted 12 min. On the second day, the mouse was re-exposed to the same context with no tone and the freezing response was monitored. Fear was assessed by measuring the percentage of time spent freezing, characterized by a crouching posture and an absence of any visible movement except breathing.

Ethical approval. All experiments were performed in compliance with all relevant ethical regulations. The experiments using post-mortem human samples were authorized by the Michigan State University (MSU) Human Research Protection Program. Informed consent for brain autopsies of Rush Religious Orders Study participants was authorized by the Rush University Medical Center Institutional Review Board. The experiments with 3×TgAD mice were authorized by the MSU Institutional Review Board and Institutional Animal Care and Use Committee. The experiments with *APP_{Swe}/$PSEN1_{dE9}$* mice were authorized by the local animal experimentation committee of the Canton de Vaud under license 3207. The committee that approved the license is the Commission cantonale pour l'expérimentation animale.

Human brain samples. Superior temporal cortex (Brodmann area 22) samples were obtained post mortem from participants in the Religious Orders Study who died with an ante-mortem clinical diagnosis of no cognitive impairment (NCI), mild cognitive impairment (MCI) or AD ($n=8$ per group) (Supplementary Table 6). Neuropsychological and clinical examinations, as well as post-mortem diagnostic evaluations, have been described elsewhere[46]. Demographic, ante-mortem cognitive testing and post-mortem diagnostic variables were compared among the groups using the non-parametric Kruskal–Wallis test with Bonferroni correction for multiple comparisons. Gender and apoE ε4 allele distribution were compared using a Fisher's exact test with Bonferroni correction.

Bioinformatics analysis. For the *in silico* analysis of human brain expression datasets, we have used two sets of publicly available RNA-seq data: (1) from the Harvard Brain Tissue Resource Center (HBTRC), for human primary visual cortex (GN accession: GN327) and human prefrontal cortex (GN accession: GN328) and (2) from the Translational Genomics Research Institute, for the whole brain (GN accession: GN314)[47]. These two datasets are publicly available on GeneNetwork (http://www.genenetwork.org/webqtl/main.py). For correlation analysis, Pearson's *r* genetic correlation of the UPR^{mt}, mitophagy, endoplasmic reticulum stress and HSR gene sets was performed to establish the correlation between these pathways and genes that are associated or are causal to the development of AD. Analyses were performed using the hallmarks and canonical pathway gene sets databases. Additional information about the datasets used are provided in Supplementary Information.

Gene expression analyses in *C. elegans*. A total of approximately 3,000 worms per condition, divided into three biological replicates, was recovered in M9 buffer from NGM plates and lysed in the TriPure RNA reagent. Each experiment was repeated twice. Total RNA was transcribed to cDNA using the QuantiTect Reverse Transcription Kit (Qiagen). Expression of selected genes was analysed using the LightCycler480 system (Roche) and LightCycler 480 SYBR Green I Master reagent (Roche). For *C. elegans*, two housekeeping genes were used to normalize the expression data, actin (*act-1*) and peroxisomal membrane protein 3 (*pmp-3*). See Supplementary Table 7 for the primer list.

Gene expression analyses in mice. Total RNA was extracted from tissues using TriPure RNA isolation reagent (Roche) according to the product manual. Expression of selected genes was analysed using the LightCycler480 system (Roche) and LightCycler 480 SYBR Green I Master reagent (Roche). The β2-microglobulin (*B2m*) gene was used as housekeeping reference. See Supplementary Table 8 for the primer list.

Gene expression analyses of human samples. Total RNA was extracted using guanidine-isothiocyanate lysis (PureLink, Ambion) from cortex samples, and RNA integrity and concentration were verified using Bioanalysis (Agilent). Samples were randomized based on diagnostic group and assayed in triplicate on a real-time PCR cycler (ABI 7500, Applied Biosystems) in 96-well optical plates. qPCR was performed using Taqman hydrolysis probe primer sets (Applied Biosystems) specific for the following human transcripts (Supplementary Table 10): *HSPA9*, *HSPD1*, *YME1L1*, *DNM1L*, *BECN1*, *SQSTM1*, *PARK2* (also known as *PRKN*), *COX5A* and *CYC1*. A primer set specific for human *GAPDH* was used as a control housekeeping transcript. For the APP_{Swe}-expressing SH-SY5Y cell line, total RNA was extracted using TriPure RNA isolation reagent, and expression of selected transcripts was analysed using the LightCycler480 system (Roche) and LightCycler 480 SYBR Green I Master reagent (Roche). The *GAPDH* gene was used as housekeeping reference. See Supplementary Table 9 for the primer list. The $\Delta\Delta C_t$ method was used to determine relative expression levels of each amplicon. Variance component analyses revealed relatively low levels of within-case variability, and the average value of the triplicate qPCR products from each case was used in subsequent analyses.

***C. elegans* strains and plasmids generation, and RNAi experiments.** *C. elegans* strains (Supplementary Table 12) were cultured at 20 °C on nematode growth medium (NGM) agar plates seeded with *E. coli* strain OP50 unless stated otherwise. Strains used in this study were the wild-type Bristol N2, GMC101 (unc-54p::A-beta-1-42::unc-54 3′-UTR + mtl-2p::GFP)[15], CL2122 ((pPD30.38) unc-54(vector) + (pCL26) mtl-2::GFP)[48], CB4876 (*clk-1*(*e2519*)) and MQ1333 (*nuo-6*(*qm200*)). Strains were provided by the *Caenorhabditis* Genetics Center (University of Minnesota). The strain CL2122 was outcrossed three times in the N2 background, and subsequently used in the control experiments reported here. AUW9 and AUW10: (GMC101 + epfEx6(*atfs-1p::atfs-1*)) and AUW11: (CL2122 + *epfEx7*(*atfs-1p::atfs-1*)) overexpression strains, and AUW12: [GMC101 + *clk-1*(*e2519*) III), AUW13: (GMC101+ *nuo-6*(*qm200*) I) were generated for this study.

Cloning and sequencing primers used for *C. elegans* analyses are listed Supplementary Table 13. The *atfs-1p::atfs-1* expression vector was created by amplifying the 1,488-bp sequence upstream of the transcription start site of the *atfs-1* coding region by using worm genomic DNA for the promoter region. The PCR product was digested with PciI and AgeI and ligated into the pPD30.38 expression vector containing the *gfp* coding sequence cloned between inserted AgeI and NotI restriction sites. The *atfs-1* coding sequence was instead amplified using *C. elegans* cDNA, and the PCR product was inserted into pPD30.38 downstream of the promoter region, between AgeI and NheI restriction sites. The correctness of the *atfs-1p::atfs-1* construct was assessed by sequencing with the indicated pPD30.38 and *atfs-1* sequencing primers. Two independent GMC101 lines (AUW9 and AUW10), and one CL2122 strain (AUW11) carrying the *atfs-1p::atfs-1* transgene as extrachromosomal array were analysed in this study. Injection marker *myo-2p::gfp* was cloned by amplifying the 1,179-bp sequence upstream of the transcription start site of the *myo-2* coding region by using *C. elegans* genomic DNA. The PCR product was digested with PciI and AgeI and ligated into the pPD30.38 expression vector containing *atfs-1::gfp* to replace the *atfs-1* promoter sequence between PciI and AgeI restriction sites. All transgenic strains were created using microinjection. For the generation of the GMC101 lines AUW12 and AUW13, GMC101 males were generated after exposure of L4 worms to 30 °C for 3 h, and allowed to mate with L4 hermaphrodites from *clk-1* or *nuo-6* mutant strains. The derived progeny was selected for homozygosis of the GMC101 intestinal GFP marker for a few generations, and the homozygosis of the *clk-1* or *nuo-6* mutant alleles verified by amplifying and sequencing a 500-bp region of the worms genomic DNA encompassing the desired mutation (Supplementary Table 13). Bacterial feeding RNAi experiments were carried out as described[49]. Clones used were *atfs-1* (ZC376.7), *ubl-5* (F46F11.4), *mrps-5* (E02A10.1), *dct-1* (C14F5.1), *daf-16* (R13H8.1), *sir-2.1* (R11A8.4), *xbp-1* (R74.3) and *hsf-1* (Y53C10A.12). Clones were purchased from GeneService and verified by sequencing. The novel *atfs-1* RNAi construct (*atfs-1* #2) used in this study was generated by amplifying 1,400 bp of the *atfs-1* genomic DNA

sequence, starting from the last exon of *atfs-1*. Gateway cloning (Thermo Scientfic) was used to insert the PCR product into the gateway vector pL4440gtwy (Addgene 11344), and verified by sequencing. *atfs-1* knockdown was verified by qPCR for all the *atfs-1* RNAi constructs used here. For phenotypic studies (see below), worms at the L4 larval stage were allowed to reach adulthood and lay eggs on the treatment plates. The derived F1 worms were shifted from 20 °C to 25 °C at the L4 stage to induce amyloid accumulation and paralysis, and phenotypes were assessed over time as indicated. For double RNAi experiments, we used a combination of *atfs-1* with *mrps-5* RNAi constructs as indicated in the text, with 80% amount of *atfs-1* and 20% *mrps-5* RNAi. For mRNA analysis, synchronized L1 worms were exposed to the treatment plates, and shifted from 20 °C to 25 °C when reaching the L4 stage. After 24-h incubation at 25 °C, corresponding to day 1 of adulthood, they were collected in M9 for analysis.

Pharmacological treatment of *C. elegans*. Doxycycline was obtained from Sigma-Aldrich and dissolved in water[23]. For experiments, a final concentration of 15 μg ml^{-1} was used. Olaparib (AZD2281) was dissolved in DMSO to experimental concentrations of 300 nM[34]. Nicotinamide riboside triflate (NR) was custom synthesized by Novalix (http://www.novalix-pharma.com/) and dissolved in water, and used at a final concentration of 1 mM[34]. Compounds were added just before pouring the plates. For phenotyping experiments, parental F0 L4 worms were allowed to reach adulthood and lay eggs on the treatment plates. The derived F1 worms were therefore exposed to compounds during the full life from eggs until death. For RNA analysis experiments, synchronized L1 worms were exposed to the compounds until collection. To ensure a permanent exposure to the compound, plates were changed twice a week.

Worm phenotypic assays. *Mobility. C. elegans* movement analysis was performed as described[16], starting from day 1 of adulthood, using the Movement Tracker software. The experiments were repeated at least twice.

Development. 50 adult worms per condition were transferred to NGM agar plates (10 worms per plate) and allowed to lay eggs for 3 h. They were then removed and the number of eggs per plate was counted. After 72 h, the number of L1–L3 larvae, L4 and adult worms was counted. The experiment was done twice with five individual plates.

Paralysis and death score. 5 L4 worms per condition were allowed to reach adulthood and lay eggs on the treatment plates. 45 to 60 F1 worms per condition were manually scored for paralysis after poking, as previously described[15]. Worms that were unable to respond to any repeated stimulation, were scored as dead. Results are representative of data obtained from at least three independent experiments.

Oxygen-consumption assays. Oxygen consumption was measured using the Seahorse XF96 equipment (Seahorse Bioscience)[34,50]. Respiration rates were normalized to the number of worms in each individual well and calculated as averaged values of 5–6 repeated measurements. Each experiment was repeated at least twice.

MitoTracker Orange CMTMRos staining. A population of 20 worms at L4 stage were transferred on plates containing MitoTracker Orange CMTMRos (Thermo Scientific) at a final concentration of 2 μg μl^{-1}. The plates were incubated at 25 °C and the worms were collected and washed in 200 μl of M9 in order to remove the residual bacteria after 24 h of treatment. The worms were then incubated for 30 min on regular NGM plates at 25 °C and mounted on an agar pad in M9 buffer for visualization. Mitochondria were observed using confocal laser microscopy.

Phalloidin and DAPI staining. A population of 100 L4 worms was incubated for 24 h at 25 °C. The worms were then washed in M9 and frozen in liquid nitrogen, immediately after this, they were lyophilized using a centrifugal evaporator. Worms were permeabilized using acetone. 2 U of phalloidin (Thermo Scientific) was resuspended in 20 μl of a buffer containing: Na-phosphate pH 7.5 (final concentration 0.2 mM), $MgCl_2$ (final concentration 1 mM), SDS (final concentration 0.004%) and dH_2O to volume. The worms were incubated for 1 h in the dark and then washed twice in PBS and incubated in 20 μl of 2 μg ml^{-1} DAPI in PBS for 5 min. Following the immobilization, worms were observed using confocal laser microscopy.

Real-time PCR for mitochondrial:nuclear DNA ratio. Absolute quantification of the mtDNA copy number in worms was performed by real-time PCR. Relative values for *nd-1* and *act-3* were compared within each sample to generate a ratio representing the relative level of mitochondrial DNA per nuclear genome. The results obtained were confirmed with a second mitochondrial gene *MTCE.26*. The average of at least three technical repeats was used for each biological data point. Each experiment was performed on at least five independent biological samples.

Cell culture and treatments. The SH-SY5Y neuroblastoma cell line expressing the APP Swedish K670N/M671L double mutation (APP_{Swe})[25] was a gift from A. Cedazo-Minguez (Karolinska Institute). Cells were grown in DMEM/F-12, supplemented with 10% fetal bovine serum (FBS, Gibco), GlutaMAX (100×, Gibco) and penicillin–streptomycin (1×, Gibco). Cells were selected in 4 μg ml^{-1} Geneticin Selective Antibiotic (G418 Sulphate, Sigma-Aldrich) and grown for three generations before experiments with cells plated and passaged at 4×10^3 cells per ml and 60% confluence, respectively. Cells were cultured at 37 °C in a 5% CO_2 atmosphere and tested for mycoplasma using Mycoprobe (CUL001B, R&D systems) following the manufacturer's instructions. Cells were treated with 10 μg ml^{-1} DOX, 1 or 3 mM NR, or 0.5 μM ISRIB (Sigma-Aldrich), as indicated for 24 h before cell collection or fixation. For immunostaining, cells were fixed with 1× Formal-Fixx (Thermo Scientific) for 15 min. After 15 min permeabilization with 0.1% Triton X-100, cells were blocked in PBS supplemented with 5% FBS for 1 h and immunostained overnight at 4 °C with the anti-β-amyloid 1–42 antibody (1:100, Millipore AB5078P). The secondary antibody was coupled to an Alexa-488 fluorochrome (Thermo Scientific) and nuclei were stained with DAPI (Invitrogen, D1306). After washing in PBS, cell slides were mounted with DAKO mounting medium (DAKO, S3023) and analysed with a Zeiss LSM 700 confocal microscope (Carl Zeiss MicroImaging) equipped with a Plan-Apochromat 40×/1.3 NA oil immersion objective lens using a 488 nm laser. Laser power was set at the lowest intensity allowing clear visualization of the signal. Imaging settings were maintained with the same parameters for comparison between different experimental conditions.

Western blot analysis (*C. elegans*). Worms were lysed by sonication with RIPA buffer containing protease and phosphatase inhibitors (Roche), and analysed by SDS–PAGE and western blot. The concentration of extracted protein was determined using the Bio-Rad Protein Assay. Proteins were detected using the following antibodies: anti-β-actin (Sigma-Aldrich), anti-tubulin (Santa Cruz), atp-5, ucr-1 (OXPHOS cocktail, Abcam), anti-β-amyloid 1–16 (6E10) (BioLegend). In addition to the housekeeping proteins, loading was monitored by ponceau red to ensure homogeneous loading. Pixel intensity was quantified using ImageJ software. Each immunoblot experiment was repeated at least twice using three biological replicates each containing approximately 1,000 worms.

Western blot analysis (mice). Frozen cortex tissue samples were lysed by mechanical homogenization with RIPA buffer containing protease and phosphatase inhibitors, and analysed by SDS–PAGE and western blot. Subsequently, the concentration of extracted protein was determined using the Bio-Rad Protein Assay. Proteins were detected using the following antibodies: HSP60 (Enzo Life Science), CLPP (Sigma-Aldrich), GAPDH (14C10) (Cell Signaling), LONP1 (Sigma-Aldrich), PINK1 (Novus Biologicals), LC3 A/B (Cell Signaling), SDHB (OXPHOS cocktail, Abcam), MTCO1 (Abcam), ubiquitin (Enzo), p62 (BD Transduction Laboratories), phopshorylated p62 (Cell Signaling), VDAC (Abcam). In addition to the housekeeping proteins, loading was monitored by ponceau red to ensure homogeneous loading. Antibody detection reactions for all immunoblot experiments were developed by enhanced chemiluminescence (Advansta) and imaged using the c300 imaging system (Azure Biosystems). Pixel intensity was quantified using ImageJ software.

Western blot analysis (human samples). Frozen cortex tissue samples were prepared as previously described[51]. Samples were randomized based on diagnostic group and assayed in triplicate. For CLPP, blots were incubated overnight at 4 °C with a mouse monoclonal antibody against CLPP (1:1,000; clone 2E1D9, ProteinTech) and then incubated for 1 h with a near-infrared-labelled goat anti-mouse IgG secondary antiserum (IRDye 800LT, 1:10,000; Licor) and analysed on an Odyssey imaging system (Licor). After imaging, the membranes were stripped and re-probed with a mouse monoclonal GAPDH antibody (1:10,000; clone 2D9, Origene) overnight followed by a 1-h incubation with near-infrared-labelled goat anti-mouse IgG secondary antiserum and Odyssey imaging. For mtDNAJ (also known as TID1), blots were incubated overnight at 4 °C with both a mouse monoclonal antibody against mtDNAJ (1:500; clone RS13, Cell Signaling) and the GAPDH antibody, followed by goat anti-mouse IgG incubation and Odyssey imaging. Signals for CLPP and mtDNAJ were normalized to GAPDH for quantitative analysis. Details about the antibodies used are listed in Supplementary Table 11.

Citrate synthase activity assay. Citrate synthase enzymatic activity was determined in mouse cortex samples and *C. elegans* using the citrate synthase assay kit (Sigma-Aldrich). Absorbance at 412 nm was recorded on a Victor X4 (PerkinElmer) with 10 readings over the 1.5-min timespan. These readings were in the linear range of enzymatic activity. The difference between baseline and oxaloacetate-treated samples was obtained and used to calculate total citrate synthase activity according to the formula provided in the manual. The obtained values were normalized to the amount of protein used for each sample.

Extraction of the mitochondrial fraction. Cortexes were placed in homogenizer glass-Teflon potter tubes with 5 ml of a buffer prepared by adding 10 ml of 0.1 M Tris–MOPS and 1 ml of EGTA-Tris to 20 ml of 1 M sucrose and bringing the volume to 100 ml with distilled water. Homogenization was performed at 1,600 r.p.m. for 5 min. The samples were then centrifuged for 10 min at 600*g* and

the supernatants were collected. A second centrifugation at 7,000*g* for 10 min was performed on the supernatants in order to precipitate the mitochondrial fraction. All steps were performed on ice or at 4 °C.

Histology. Brain hemispheres were collected from anaesthetized mice and immediately frozen in isopentane. 8-μm cryosections were collected and fixed with 4% paraformaldehyde. For immunostaining, sections were stained with 0.01% thioflavin S (Sigma-Aldrich) for 15 min at room temperature, and after washes in ethanol and PBS, stained with Hoechst (Life Technology). After washing in PBS, tissue sections were mounted with DAKO mounting medium. Images were acquired using a Leica DM 5500 (Leica Microsystems) CMOS camera 2900 Colour at the same exposure time. Quantitative analysis of the immunofluorescence data was carried out by histogram analysis of the fluorescence intensity at each pixel across the images using ImageJ (Fiji; National Institutes of Health). Appropriate thresholds were used for all images of each single experiment to eliminate the background signal in the images before histogram analysis. Fluorescence intensity and signal-positive areas were calculated using the integrated 'analyse particles' tool of the Fiji software, and statistical analysis was performed using Prism 6 (GraphPad Software).

Statistical analyses. No statistical methods were used to predetermine sample size. Differences between two groups were assessed using two-tailed *t*-tests. Differences between more than two groups were assessed by using two-way ANOVA. GraphPad Prism 6 (GraphPad Software, Inc.) was used for all statistical analyses. Variability in all plots and graphs is presented as the s.e.m. All $P < 0.05$ were considered to be significant. $*P < 0.05$; $**P \leq 0.01$; $***P \leq 0.001$; $****P \leq 0.0001$ unless stated otherwise. All mouse experiments were performed once. Animals that showed signs of severity, predefined by the animal authorizations were euthanized. These animals, together with those who died spontaneously during the experiments, were excluded from the calculations. These criteria were established before starting the experiments. For motility, fitness and death scoring experiments in *C. elegans*, sample size was estimated based on the known variability of the assay. All experiments were done non-blinded and repeated at least twice.

Data availability. All data generated or analysed during this study are included in this published article (and its Supplementary Information). Source data for uncropped gels are provided in Supplementary Fig. 1 and Source Data for all the individual *P* values are provided in the online version of the paper. The expression datasets that support the findings of this study are available in GeneNetwork (http://www.genenetwork.org/webqtl/main.py) with identifiers GN327, GN328, GN314[47], and from the GEO database (https://www.ncbi.nlm.nih.gov/geo/) with the identifiers GSE3112, GSE39454[52,53]. The worm strains generated in this study are available upon request from the corresponding author.

46. Tiernan, C. T. *et al.* Protein homeostasis gene dysregulation in pretangle-bearing nucleus basalis neurons during the progression of Alzheimer's disease. *Neurobiol. Aging* **42,** 80–90 (2016).
47. Liang, W. S. *et al.* Alzheimer's disease is associated with reduced expression of energy metabolism genes in posterior cingulate neurons. *Proc. Natl Acad. Sci. USA* **105,** 4441–4446 (2008).
48. Fonte, V. *et al.* Suppression of *in vivo* β-amyloid peptide toxicity by overexpression of the HSP-16.2 small chaperone protein. *J. Biol. Chem.* **283,** 784–791 (2008).
49. Kamath, R. S., Martinez-Campos, M., Zipperlen, P., Fraser, A. G. & Ahringer, J. Effectiveness of specific RNA-mediated interference through ingested double-stranded RNA in *Caenorhabditis elegans*. *Genome Biol.* **2,** RESEARCH0002 (2001).
50. Koopman, M. *et al.* A screening-based platform for the assessment of cellular respiration in *Caenorhabditis elegans*. *Nat. Protoc.* **11,** 1798–1816 (2016).
51. Counts, S. E., Nadeem, M., Lad, S. P., Wuu, J. & Mufson, E. J. Differential expression of synaptic proteins in the frontal and temporal cortex of elderly subjects with mild cognitive impairment. *J. Neuropathol. Exp. Neurol.* **65,** 592–601 (2006).
52. Greenberg, S. A. *et al.* Plasma cells in muscle in inclusion body myositis and polymyositis. *Neurology* **65,** 1782–1787 (2005).
53. Zhu, W. *et al.* Genomic signatures characterize leukocyte infiltration in myositis muscles. *BMC Med. Genomics* **5,** 53 (2012).

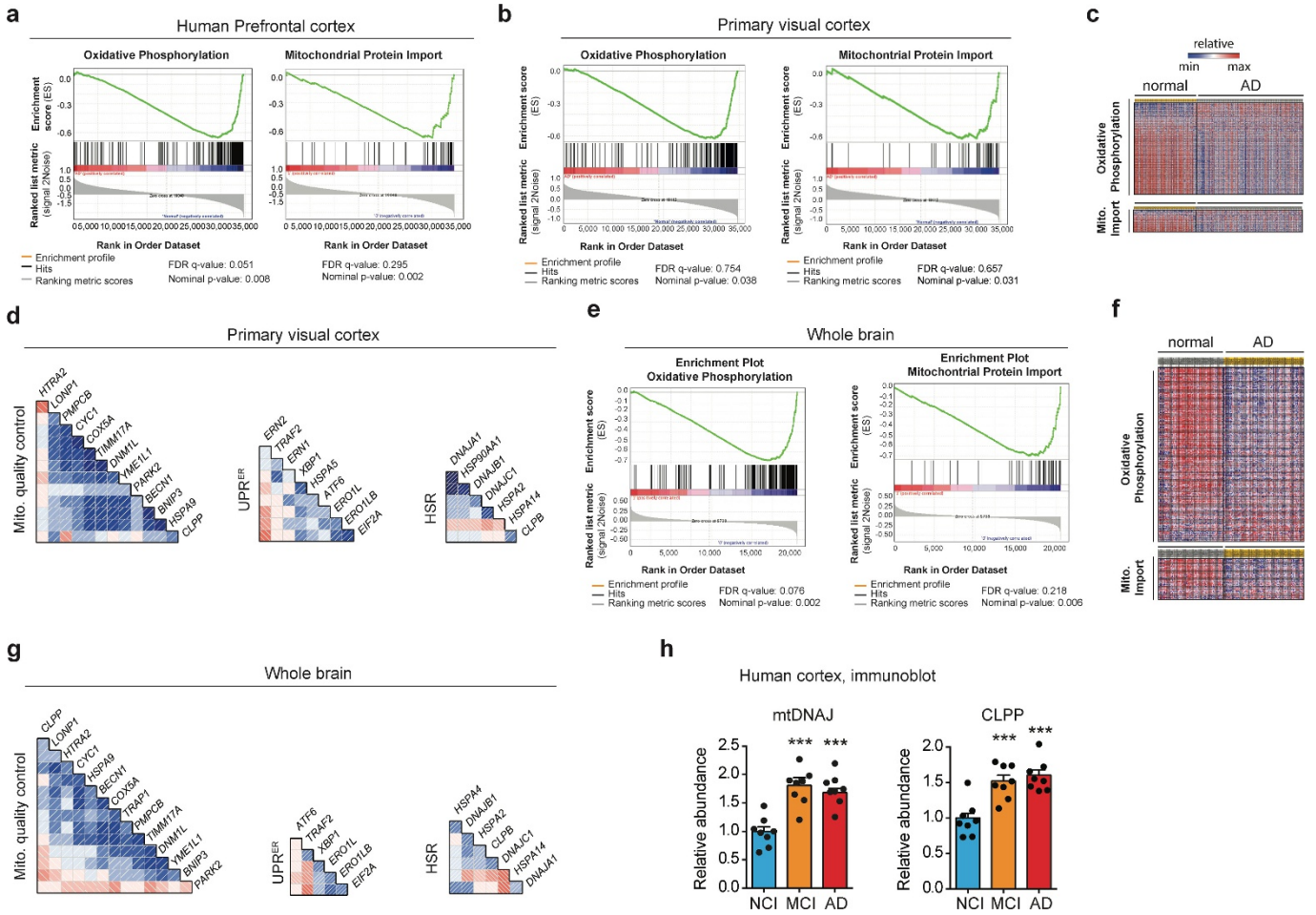

Extended Data Figure 1 | Mitochondrial function pathways are disrupted in patients with AD. a, Gene set enrichment analysis of OXPHOS (false-discovery rate (FDR) = 0.051, nominal $P = 0.008$) and mitochondrial import (FDR = 0.295, nominal-$P = 0.002$) genes in human prefrontal cortex of patients with AD (GN328; healthy, $n = 195$; AD, $n = 388$ individuals). **b**, **e**, Gene set enrichment analysis of OXPHOS and mitochondrial import genes in human visual cortex (**b**) (GN327; healthy, $n = 195$; AD, $n = 388$) and whole brain (**e**) (GN314, $n = 16$ healthy individuals and 33 individuals with AD) of patients with AD. **b**, FDR = 0.754, $P = 0.038$ for OXPHOS, FDR = 0.657, $P = 0.031$ for mitochondrial import. **e**, FDR = 0.076, $P = 0.002$ for OXPHOS, FDR = 0.218, $P = 0.006$ for mitochondrial import. **c**, **f**, Heat maps of genes from visual cortex (**c**) and whole brain (**f**) datasets. **d**, **g**, Correlation plots of mitochondrial stress genes, UPR^{ER} and HSR levels in human visual cortex (**d**) and whole brain (**g**) from patients with AD. For further information, see Supplementary Table 5. **h**, Quantification of immunoblots of mtDNAJ and CLPP ($n = 8$ per group shown in Fig. 1d) from brains of humans with no cognitive impairment (NCI), mild-cognitive impairment (MCI) and mild to moderate AD. This experiment was performed independently twice. Data are mean ± s.e.m. $^{***}P \leq 0.001$. Differences were assessed using two-tailed *t*-tests (95% confidence interval). Mito., mitochondrial. For all individual *P* values, see Source Data.

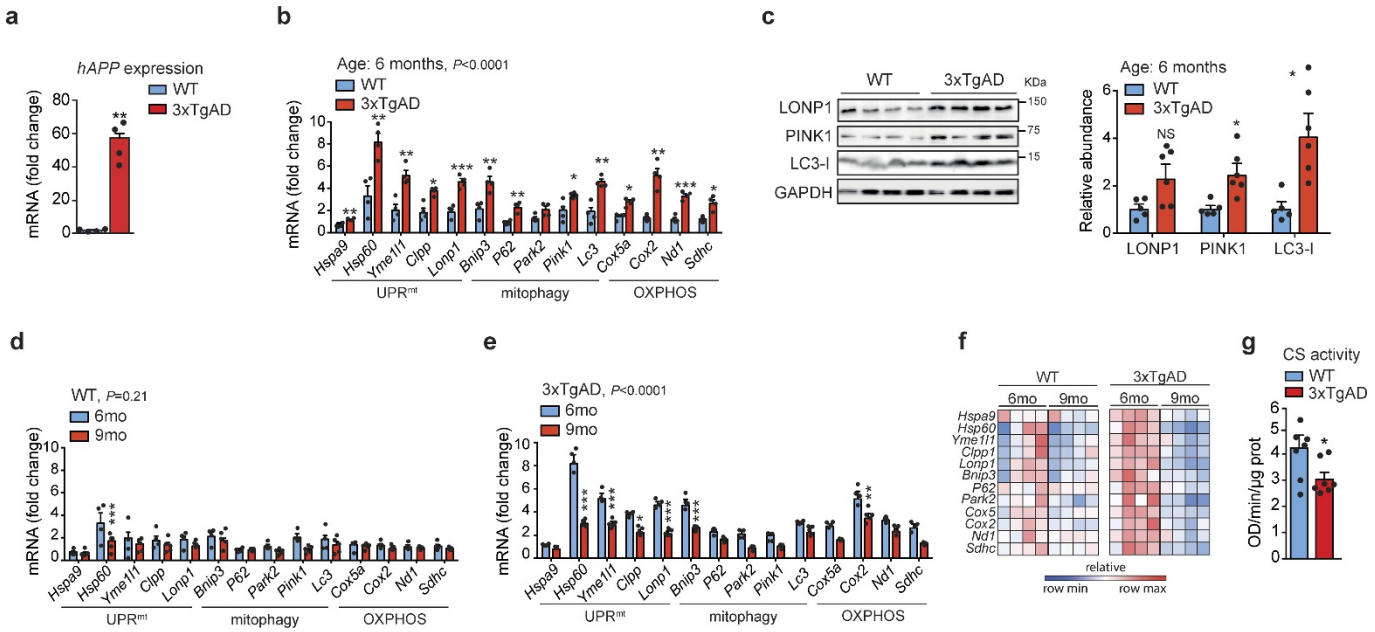

Extended Data Figure 2 | MSR analysis and mitochondrial function in 3×TgAD mice. a, Human *APP* expression in cortex tissues of wild-type and 3×TgAD mice ($n = 4$ mice per group). $^{**}P = 0.002$. **b**, MSR transcript analysis from cortex tissues of wild-type ($n = 4$ mice) and 3×TgAD ($n = 4$ mice) mice at six months of age. **c**, Immunoblot analysis (wild-type, $n = 5$; 3×TgAD, $n = 6$, western blot of four representative mice) and quantification of the samples as in **b**. $^{*}P < 0.05$. ($P = 0.035$, $P = 0.029$). **d**–**f**, MSR transcript analysis from cortex tissues of wild-type (**d**; 6 months, $n = 4$ mice; 9 months, $n = 5$ mice) and 3×TgAD (**e**; 6 months, $n = 4$ mice; 9 months, $n = 5$ mice) mice at six and nine months of age, and corresponding heat maps (**f**) representing relative variation in gene expression between groups. **g**, Citrate synthase activity assay in cortex tissues from wild-type and 3×TgAD mice (wild-type, $n = 8$ mice; 3×TgAD, $n = 7$ mice). $^{*}P = 0.039$. Data are mean ± s.e.m. $^{*}P < 0.05$; $^{**}P \leq 0.01$; $^{***}P \leq 0.001$; n.s., not significant. Overall differences between conditions were assessed by two-way ANOVA. Differences in individual genes, proteins or between two groups were assessed using two-tailed *t*-tests (95% confidence interval). All experiments were performed independently twice. For uncropped gel source data, see Supplementary Fig. 1. For all individual *P* values, see Source Data.

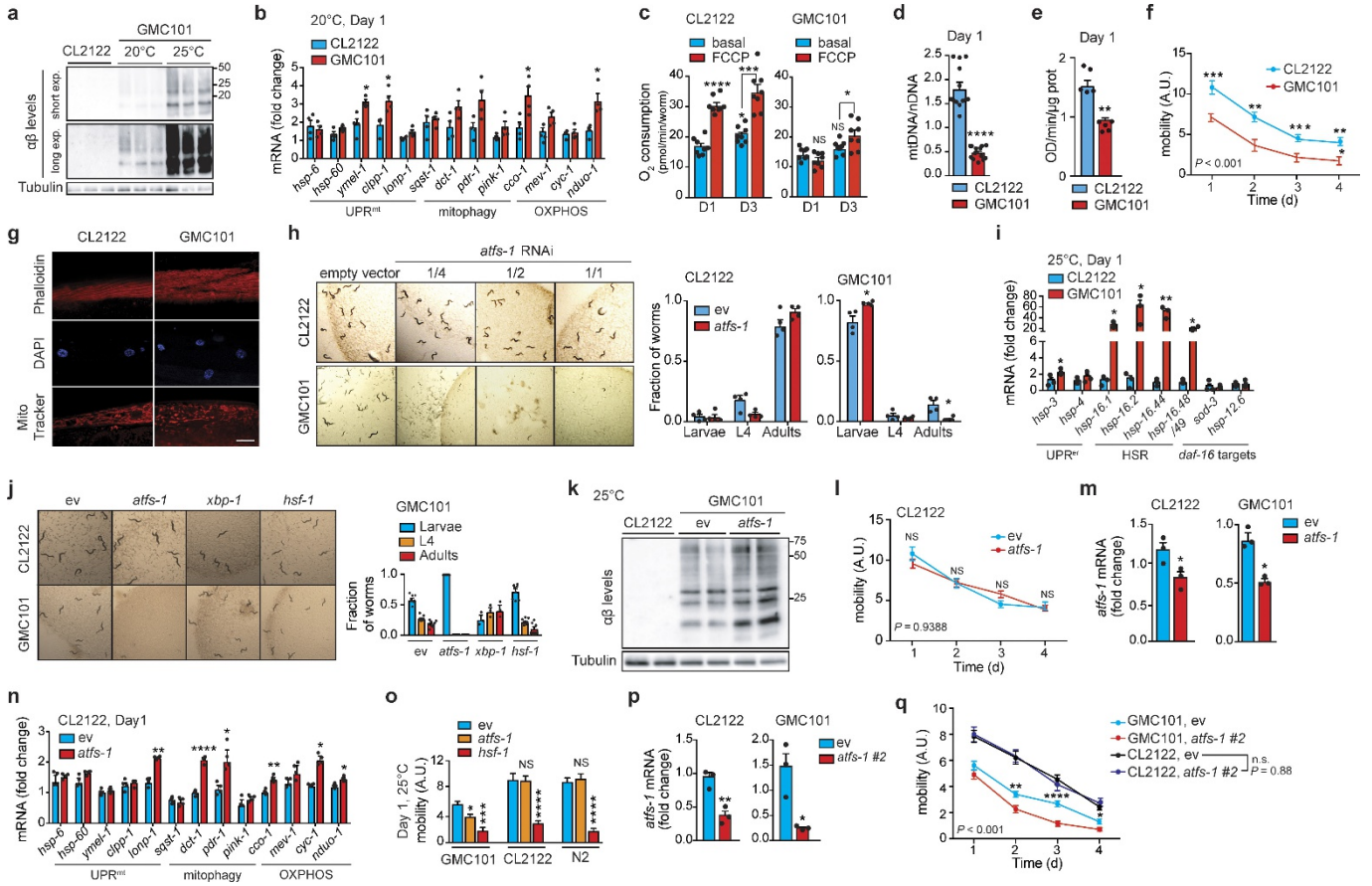

Extended Data Figure 3 | Characterization of Aβ proteotoxicity and stress response pathways in GMC101 worms. a, Amyloid aggregation in CL2122 and GMC101 worms ($n = 3$ biologically independent samples) at 20 °C or 25 °C. **b**, MSR transcript analysis in worms at 20 °C ($n = 3$ biologically independent samples). **c**, Respiration assay in CL2122 and GMC101 worms (CL2122, $n = 8$; GMC101, $n = 8$ biologically independent samples). **d**, mitochondrial:nuclear DNA ratio in CL2122 and GMC101 worms ($n = 13$ animals per group). **e**, Citrate synthase activity in CL2122 and GMC101 worms on D1 ($n = 5$ biologically independent samples). $^{**}P = 0.004$. **f**, CL2122 and GMC101 mobility (CL2122, $n = 48$; GMC101, $n = 59$ worms). **g**, Confocal images of D1 adult worms showing muscle cell integrity, nuclear morphology and mitochondrial networks. Scale bar, 10 μm. See Methods. **h**, Representative images and fraction of worms in different stages of development upon *atfs-1* RNAi ($n = 4$ independent experiments). $^{*}P < 0.05$ (larvae, $P = 0.048$; adults, $P = 0.035$). **i**, Transcript analysis of UPR^{ER}, HSR and *daf-16* target genes ($n = 3$ biologically independent samples). **j**, Representative images and fraction of worms in different stages of development fed with *atfs-1*, *xbp-1* and *hsf-1* RNAis at 20 °C ($n = 8$ per group; *xbp-1*, $n = 3$ biologically independent samples). **k**, Amyloid aggregation upon *atfs-1* RNAi ($n = 2$ biological replicates). **l**, Mobility of CL2122 fed with 50% dilution of *atfs-1* RNAi (ev, $n = 48$; *atfs-1* 1/2, $n = 47$ worms). **m**, Validation of the efficacy of *atfs-1* RNAi in CL2122 and GMC101 worms ($n = 3$ biologically independent samples). **n**, MSR transcript analysis of CL2122 worms upon *atfs-1* RNAi ($n = 3$ biologically independent samples). **o**, Mobility of D1 adult worms fed with *atfs-1* or *hsf-1* RNAi at 25 °C (CL2122, ev, $n = 22$; *atfs-1*, $n = 27$; *hsf-1*, $n = 28$; GMC101, ev, $n = 27$; *atfs-1*, $n = 21$; *hsf-1*, $n = 18$; N2, ev, $n = 31$; *atfs-1*, $n = 38$; *hsf-1*, $n = 27$ worms). **p**, Validation of the efficacy of the newly generated *atfs-1* #2 RNAi ($n = 3$ biologically independent samples). For further information, see Methods. **q**, Worm mobility upon *atfs-1* #2 RNAi (CL2122, ev, $n = 47$; *atfs-1* #2, $n = 42$; GMC101, ev, $n = 55$; *atfs-1* #2, $n = 46$ worms). ev, scrambled RNAi; A.U., arbitrary units. Data are mean ± s.e.m. $^{*}P < 0.05$; $^{**}P \leq 0.01$; $^{***}P \leq 0.001$; $^{****}P \leq 0.0001$; n.s., not significant. Overall differences between conditions were assessed by two-way ANOVA. Differences in individual genes or between two groups were assessed using two-tailed *t*-tests (95% confidence interval). All experiments were performed independently at least twice. For uncropped gel source data, see Supplementary Fig. 1. For all individual *P* values, see Source Data.

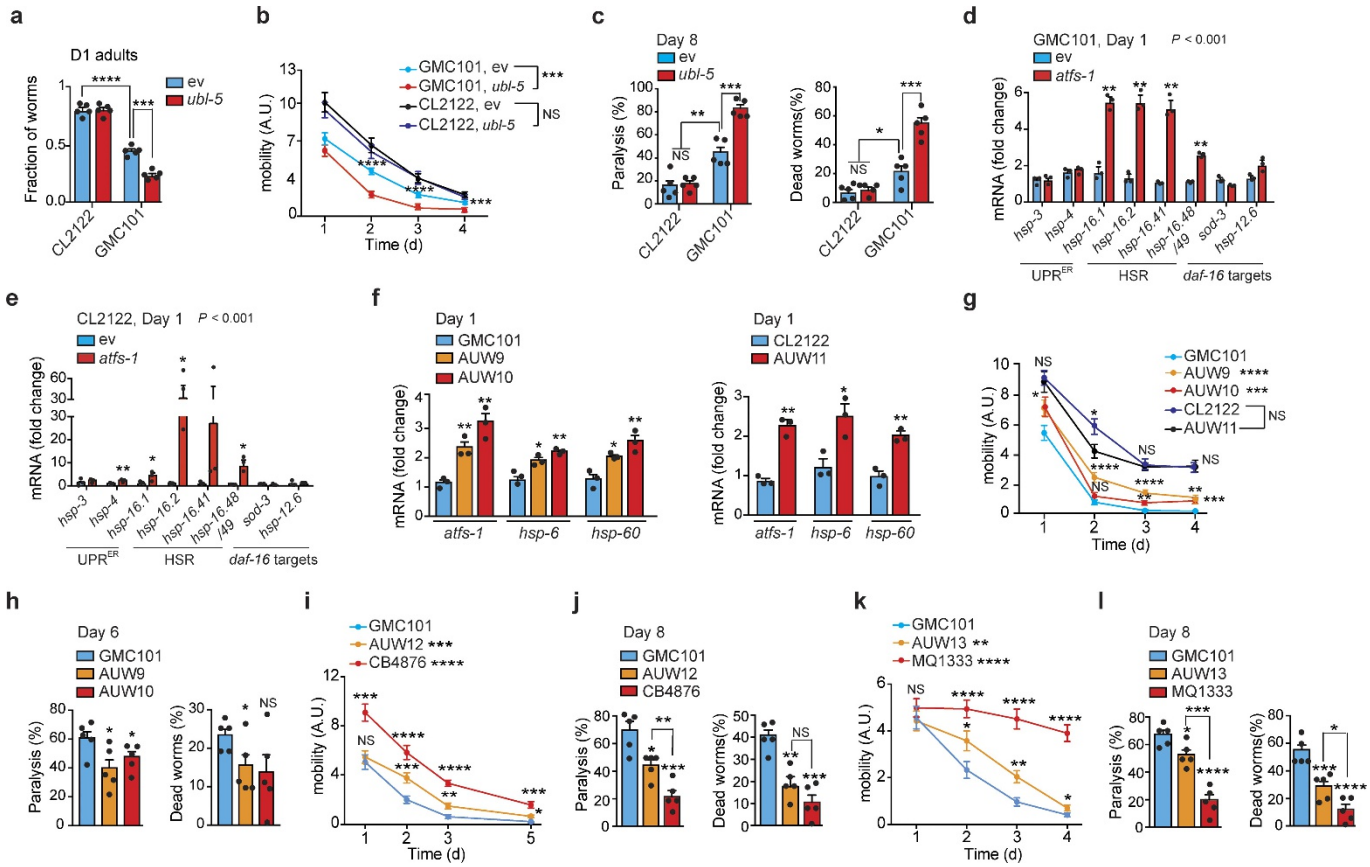

Extended Data Figure 4 | Reliance on *ubl-5* and on increased mitochondrial stress response of GMC101 worms. a, Fraction of worms that reached D1 adulthood fed with *ubl-5* RNAi ($n = 5$ biologically independent samples). **b**, **c**, Mobility of worms (**b**) and percentage of paralysed and dead D8 adult worms (**c**) upon *ubl-5* RNAi (**b**; CL2122, ev, $n = 39$; *ubl-5*, $n = 43$; GMC101, ev, $n = 40$; *ubl-5*, $n = 41$ worms; c; $n = 5$ biologically independent samples). **d**, **e**, Transcript analysis of UPR^{ER}, HSR and *daf-16* target genes in GMC101 (**d**) and CL2122 (**e**) worms upon *atfs-1* RNAi ($n = 3$ biologically independent samples). **f**, Validation of the *atfs-1*-overexpressing strains AUW9, AUW10 and AUW11 ($n = 3$ biologically independent samples). See Methods. **g**, Worm mobility in *atfs-1*-overexpressing CL2122- and GMC101-derived lines (CL2122, $n = 40$; GMC101, $n = 57$; AUW9, $n = 40$; AUW10, $n = 38$; AUW11, $n = 42$ worms). **h**, Percentage of paralysed and dead D6 adult worms ($n = 5$ biologically independent samples). $^*P < 0.05$ (from left to right, $P = 0.019$, 0.046, 0.041). **i**, **j**, Mobility (**i**) and percentage of paralysed and dead D8 adult worms (**j**) of GMC101, *clk-1* mutant (CB4876) and AUW12 strains (**i**; GMC101, $n = 35$; CB4876, $n = 42$; AUW12, $n = 38$ worms; **j**; **n** = 5 biologically independent samples). **k**, **l**, Mobility (**k**) and percentage of paralysed and dead D8 adult worms (**l**) of GMC101, *nuo-6* mutant (MQ1333) and AUW13 strains (**k**; GMC101, $n = 46$; MQ1333, $n = 50$; AUW13, $n = 47$ worms; l; $n = 5$ biologically independent samples). For further information on all strains, see Methods. ev, scrambled RNAi; A.U., arbitrary units. Data are mean ± s.e.m. $^*P < 0.05$; $^{**}P \leq 0.01$; $^{***}P \leq 0.001$; $^{****}P \leq 0.0001$; n.s., not significant. Overall differences between conditions were assessed by two-way ANOVA. Differences in individual genes or between two groups were assessed using two-tailed *t*-tests (95% confidence interval). All experiments were performed independently at least twice. For uncropped gel source data, see Supplementary Fig. 1. For all individual *P* values, see Source Data.

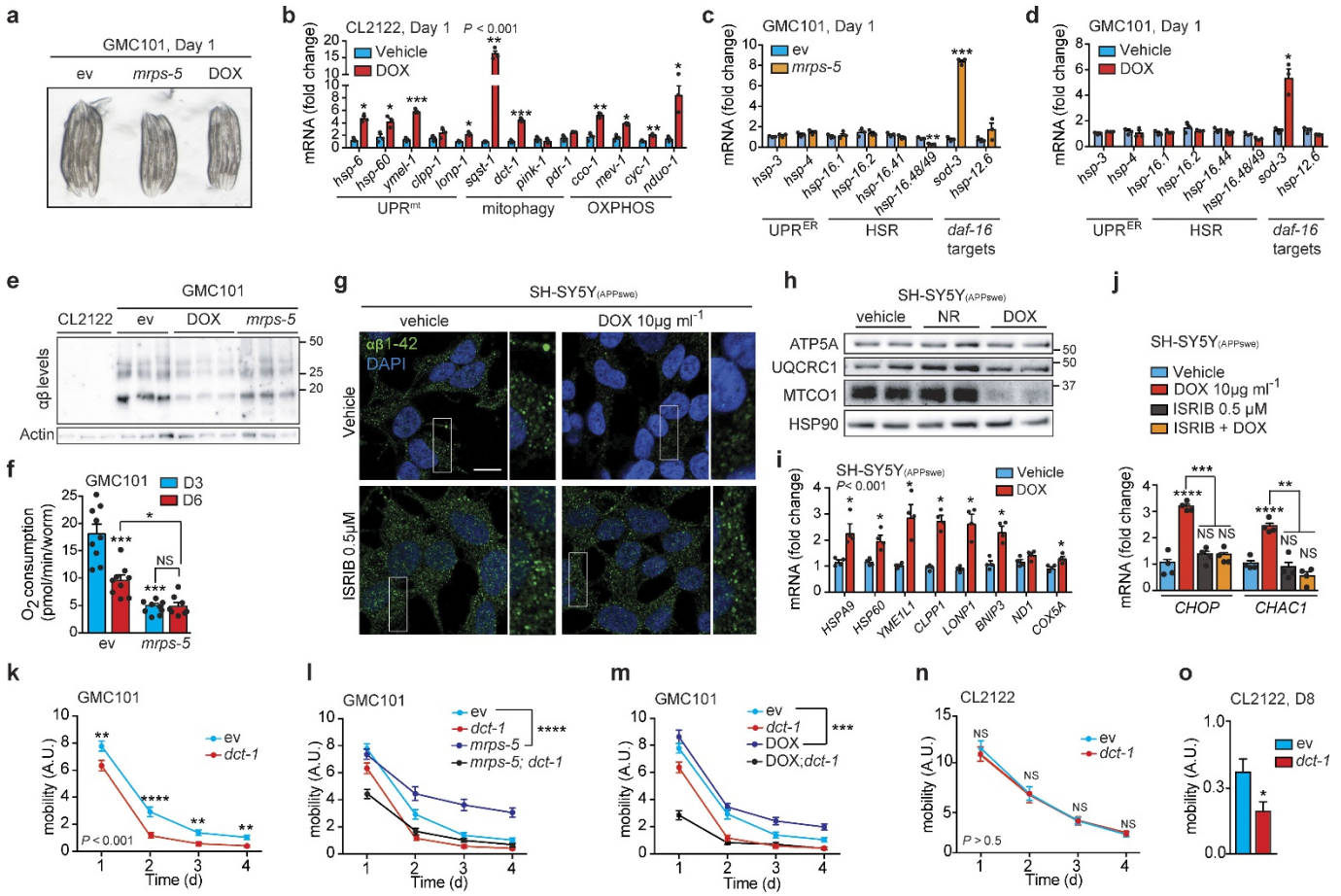

Extended Data Figure 5 | Effects of the inhibition of mitochondrial translation and mitophagy in worms, and of compound treatments in mammalian cells. a, Representative images of GMC101 worms upon *mrps-5* RNAi feeding or DOX treatment (15 μg ml^{-1}) from eggs to D1 ($n = 2$ independent experiments). **b**, MSR transcript analysis of DOX-treated CL2122 worms ($n = 4$ biologically independent samples). **c**, **d**, Transcript analysis of UPR^{ER}, HSR and *daf-16* target genes in GMC101 worms fed with *mrps-5* RNAi (**c**) or treated with DOX (15 μg ml^{-1}) (**d**) (**c**, **d**, $n = 3$ biologically independent samples). **e**, Amyloid aggregation in worms upon *mrps-5* RNAi or DOX treatment ($n = 3$ biologically independent samples). **f**, Respiration on D3 and D6 in GMC101 worms fed with *mrps-5* RNAi ($n = 9$; *mrps-5* D6, $n = 8$ biologically independent samples). **g**, Additional confocal images of the SH-SY5Y(APP$_{Swe}$) cells stained with the anti-β-amyloid 1–42 antibody, after DOX and ISRIB treatment. Scale bar, 10 μm. **h**, Immunoblot of OXPHOS proteins in SH-SY5Y(APP$_{Swe}$) cells showing the effects of NR (1 mM) and DOX (10 μg ml^{-1}) ($n = 2$ biologically independent samples). **i**, **j**, Transcript levels of MSR and OXPHOS genes (**i**) and ATF4 target genes (**j**) in APP$_{Swe}$-expressing cell line after 24 h of DOX (10 μg ml^{-1}; $n = 4$ biologically independent samples). **k**, Mobility of GMC101 worms upon *dct-1* RNAi (ev, $n = 54$; *dct-1*, $n = 44$ worms). **l**, Mobility of GMC101 worms fed with *dct-1*, *mrsp-5* or both RNAis (ev, $n = 54$; *dct-1*, $n = 44$; *mrps-5*, $n = 35$; *mrps-5*;*dct-1*, $n = 45$ worms). **m**, Mobility of GMC101 worms treated with DOX and/or fed *dct-1* RNAi (ev, $n = 54$; *dct-1*, $n = 44$; DOX, $n = 52$; DOX and *dct-1*, $n = 54$ worms). **n**, **o**, Mobility of CL2122 worms fed with *dct-1* RNAi (**n**) from D1 to D4 (ev, $n = 44$; *dct-1*, $n = 40$ worms) or (**o**) at D8 ($n = 38$ worms, $^*P < 0.05$ ($P = 0.018$)). ev, scrambled RNAi; DOX, doxycycline; NR, nicotinamide riboside; ISRIB, integrated stress response inhibitor; A.U. Data are mean ± s.e.m. $^*P < 0.05$; $^{**}P \leq 0.01$; $^{***}P \leq 0.001$; $^{****}P \leq 0.0001$; n.s., not significant. Overall differences between conditions were assessed by two-way ANOVA. Differences in individual genes or between two groups were assessed using two-tailed *t*-tests (95% confidence interval). All experiments were performed independently at least twice. For uncropped gel source data, see Supplementary Fig. 1. For all individual *P* values, see Source Data.

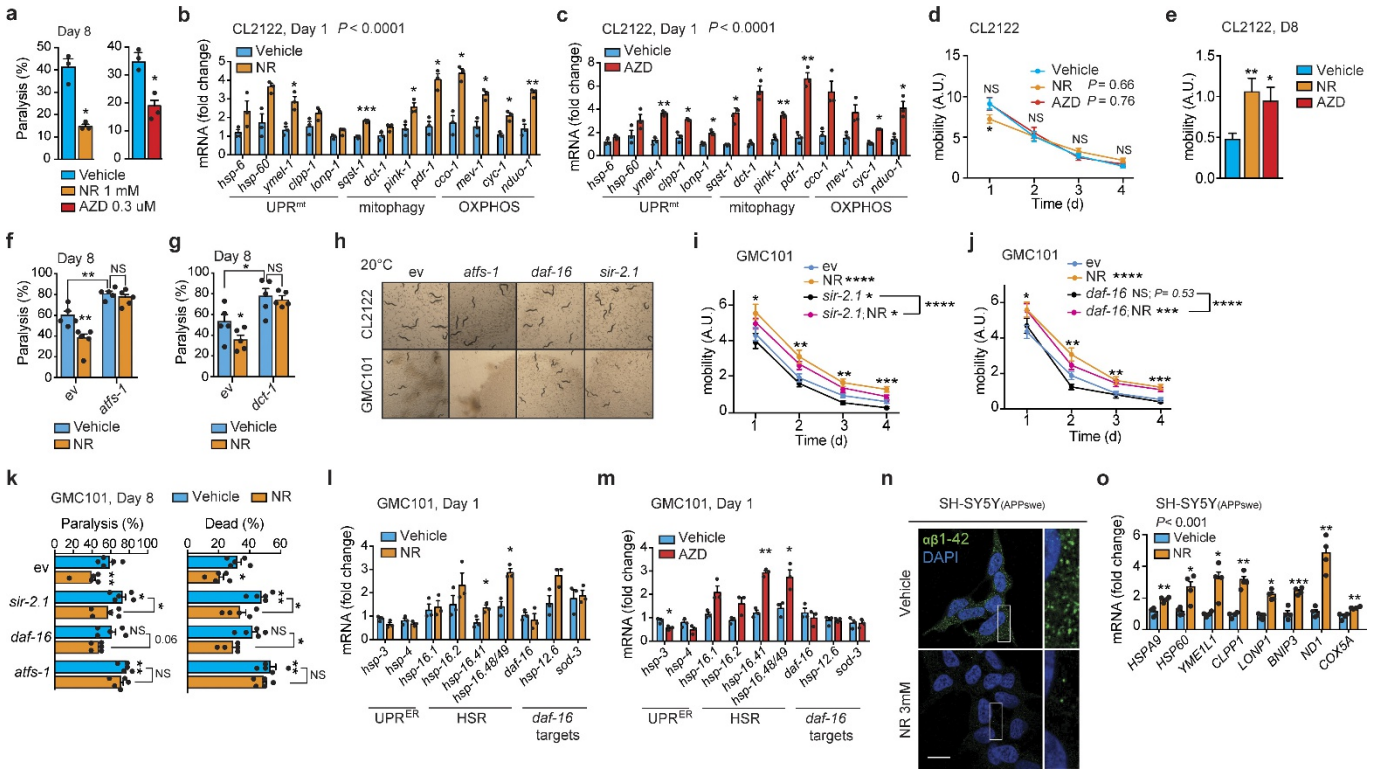

Extended Data Figure 6 | Effect of NAD$^+$-boosting compounds and sirtuin depletion in worms, and NR treatment in mammalian cells. a, Percentage of paralysed D8 adult GMC101 worms after NR or AZD treatment ($n = 3$ independent experiments). **b**, **c**, MSR transcript analysis of CL2122 worms treated with NR (**b**; 1 mM) or AZD (**c**; 0.3 μM) (**b**, **c**, $n = 3$ biologically independent samples). **d**, **e**, Mobility of CL2122 treated with NR (1 mM) or AZD (0.3 μM) from (**d**) D1 to D4 (vehicle, $n = 44$; NR, $n = 48$; AZD, $n = 43$ worms) or (**e**) at D8 (vehicle, $n = 38$; NR, $n = 36$; AZD, $n = 33$ worms, $^*P < 0.05$ ($P = 0.017$); $^{**}P \leq 0.01$ ($P = 0.004$)). **f**, **g**, Percentage of paralysed D8 adult GMC101 treated with NR upon *atfs-1* RNAi (**f**) or *dct-1* RNAi (**g**) ($n = 5$ biologically independent samples). **h**, Representative images of worms fed with *atfs-1*, *sir-2.1* or *daf-16* RNAis ($n = 2$ independent experiments). **i**, Mobility of NR-treated GMC101 worms (1 mM) fed with *sir-2.1* RNAi (ev, $n = 52$; *sir-2.1*, $n = 37$; NR, $n = 40$; *sir-2.1* and NR, $n = 51$ worms). **j**, Mobility of NR-treated GMC101 worms (1 mM) fed with *daf-16* RNAi (ev, $n = 52$; *daf-16*, $n = 43$; NR, $n = 40$; *daf-16* and NR, $n = 48$ worms). **k**, Percentage of paralysed and dead D8 adult GMC101 worms treated with NR or fed with *sir-2.1*, *daf-16* or *atfs-1* RNAis ($n = 5$ biologically independent samples). **l**, **m**, Transcript analysis of UPR^{ER}, HSR and *daf-16* target genes in GMC101 worms treated with NR (**l**; 1 mM, $^*P < 0.05$ (*hsp-16.41*, $P = 0.03$; *hsp-16.48/49*, $P = 0.008$)), or AZD (**m**; 0.3 μM, $^*P < 0.05$ ($P = 0.033$); $^{**}P \leq 0.01$ ($P = 0.0004$)) ($n = 3$ biologically independent samples). **n**, Additional confocal images of the intracellular amyloid deposits in the SH-SY5Y(APP$_{Swe}$) cells after 24 h NR treatment. **o**, Transcript levels of MSR genes in APP$_{Swe}$-expressing cells after NR (1 mM) ($n = 4$ biologically independent samples). NR, nicotinamide riboside; ISRIB, integrated stress response inhibitor; AZD, Olaparib; ev, scrambled RNAi; A.U., arbitrary units. Data are mean ± s.e.m. $^*P < 0.05$; $^{**}P \leq 0.01$; $^{***}P \leq 0.001$; $^{****}P \leq 0.0001$; n.s., not significant. Overall differences between conditions were assessed by two-way ANOVA. Differences in individual genes or between two groups were assessed using two-tailed *t*-tests (95% confidence interval). All experiments were performed independently twice. For all individual *P* values, see Source Data.

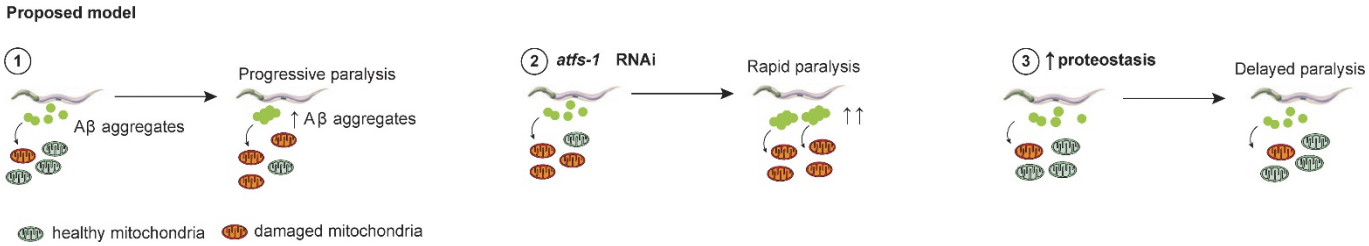

Extended Data Figure 7 | Proposed model. Scheme illustrating the role of mitochondrial proteostasis in Aβ proteopathies based on our studies in the GMC101 model. (1) Accumulation of amyloid aggregates triggers mitochondrial dysfunction, which induces the MSR. (2) *atfs-1* depletion results in loss of mitochondrial homeostasis, more pronounced amyloid aggregation and decreased healthspan. (3) Enhancing mitochondrial proteostasis with DOX, *mrps-5* RNAi, and NAD^+ boosters (NR and Olaparib) increases organismal fitness, delaying the development of Aβ proteotoxicity.

nature research

Corresponding author(s): Beili Wu, Qiang Zhao

☐ Initial submission ☐ Revised version ☒ Final submission

Life Sciences Reporting Summary

Nature Research wishes to improve the reproducibility of the work that we publish. This form is intended for publication with all accepted life science papers and provides structure for consistency and transparency in reporting. Every life science submission will use this form; some list items might not apply to an individual manuscript, but all fields must be completed for clarity.

For further information on the points included in this form, see Reporting Life Sciences Research. For further information on Nature Research policies, including our data availability policy, see Authors & Referees and the Editorial Policy Checklist.

Experimental design

1. Sample size

Describe how sample size was determined.

Due to radiation damage, X-ray diffraction data collection of the protein crystals was limited to 5-10 degree per crystal. To collect a complete data set for structure determination, diffraction data from multiple crystals were integrated and scaled using XDS. By calculating completeness of the data set, diffraction data from 10 crystals were used to ensure the completeness was close to 100%.

2. Data exclusions

Describe any data exclusions.

No data were excluded from the analyses.

3. Replication

Describe whether the experimental findings were reliably reproduced.

All attempts at replication were successful.

4. Randomization

Describe how samples/organisms/participants were allocated into experimental groups.

Randomization is not relevant to this study, as protein and crystal samples are not required to be allocated into experimental groups in protein structural studies, and no animals or human research participants are involved in this study.

5. Blinding

Describe whether the investigators were blinded to group allocation during data collection and/or analysis.

Blinding is not relevant to this study, as protein and crystal samples are not required to be allocated into experimental groups in protein structural studies, and no animals or human research participants are involved in this study.

Note: all studies involving animals and/or human research participants must disclose whether blinding and randomization were used.

6. Statistical parameters

For all figures and tables that use statistical methods, confirm that the following items are present in relevant figure legends (or in the Methods section if additional space is needed).

n/a	Confirmed	
☐	☒	The exact sample size (*n*) for each experimental group/condition, given as a discrete number and unit of measurement (animals, litters, cultures, etc.)
☐	☒	A description of how samples were collected, noting whether measurements were taken from distinct samples or whether the same sample was measured repeatedly
☐	☒	A statement indicating how many times each experiment was replicated
☒	☐	The statistical test(s) used and whether they are one- or two-sided (note: only common tests should be described solely by name; more complex techniques should be described in the Methods section)
☒	☐	A description of any assumptions or corrections, such as an adjustment for multiple comparisons
☒	☐	The test results (e.g. *P* values) given as exact values whenever possible and with confidence intervals noted
☐	☒	A clear description of statistics including central tendency (e.g. median, mean) and variation (e.g. standard deviation, interquartile range)
☐	☒	Clearly defined error bars

See the web collection on statistics for biologists for further resources and guidance.

Software

Policy information about availability of computer code

7. Software

Describe the software used to analyze the data in this study.	GraphPad Prism: Prism 7 for Mac OS X (Version 7.0a, April 2, 2016); LabVIEW program 'LongDistances': v.593, released September 14, 2017, LabVIEW 2015 (http://www.biochemistry.ucla.edu/biochem/Faculty/Hubbell/).

For manuscripts utilizing custom algorithms or software that are central to the paper but not yet described in the published literature, software must be made available to editors and reviewers upon request. We strongly encourage code deposition in a community repository (e.g. GitHub). *Nature Methods* guidance for providing algorithms and software for publication provides further information on this topic.

Materials and reagents

Policy information about availability of materials

8. Materials availability

Indicate whether there are restrictions on availability of unique materials or if these materials are only available for distribution by a for-profit company.	No unique materials were used.

9. Antibodies

Describe the antibodies used and how they were validated for use in the system under study (i.e. assay and species).	No antibodies were used.

10. Eukaryotic cell lines

a. State the source of each eukaryotic cell line used.	CHO-K1 cells were obtained from American Type Culture Collection (ATCC).
b. Describe the method of cell line authentication used.	The CHO-K1 cell line was authenticated using a PCR based multiplex assay based on the use of short tandem repeats (STR) (Anthentication of Human Cell Lines: Standardization of STR Profiling, ANSI/ATCC ASN-0002-2011).
c. Report whether the cell lines were tested for mycoplasma contamination.	The cell line was negative for mycoplasma contamination.
d. If any of the cell lines used are listed in the database of commonly misidentified cell lines maintained by ICLAC, provide a scientific rationale for their use.	No commonly misidentified cell lines were used.

Animals and human research participants

Policy information about studies involving animals; when reporting animal research, follow the ARRIVE guidelines

11. Description of research animals

Provide details on animals and/or animal-derived materials used in the study.	No animals were used.

Policy information about studies involving human research participants

12. Description of human research participants

Describe the covariate-relevant population characteristics of the human research participants.	The study did not involve human research participants.